Solid-State Phase Transformation and Self-Assembly of Amorphous Nanoparticles into Higher-Order Mineral Structures

Stanislas von Euw, Thierry Azaïs, Viacheslav Manichev, Guillaume Laurent, Gérard Pehau-Arnaudet, Margarita Rivers, Nagarajan Murali, Daniel J Kelly, Paul G Falkowski

HAL Id: hal-03151601

https://hal.sorbonne-universite.fr/hal-03151601v1

Submitted on 24 Feb 2021

Title: Solid-state phase transformation and self-assembly of amorphous nanoparticles into higher-order mineral structures

Authors: Stanislas Von Euw[1,7]*, Thierry Azaïs[2], Viacheslav Manichev[3,4], Guillaume Laurent[2], Gérard Pehau-Arnaudet[5], Margarita Rivers[4,6], Nagarajan Murali[3], Daniel J. Kelly[7], Paul G. Falkowski[1,3]*

[1]Environmental Biophysics and Molecular Ecology Program, Department of Marine and Coastal Sciences, Rutgers University, 71 Dudley Road, New Brunswick, New Jersey, 08901, United States.

[2]Laboratoire de Chimie de la Matière Condensée de Paris, Sorbonne Université, CNRS, 4 place Jussieu, F-75005, Paris, France.

[3]Department of Chemistry and Chemical Biology, Rutgers University, 123 Bevier Road, Piscataway, New Jersey, 08854, United States.

[4]Institute of Advanced Materials, Devices, and Nanotechnology, Rutgers University, 607 Taylor Road, Piscataway, New Jersey, 08854, United States.

[5]UMR 3528 and UTech UBI, Institut Pasteur, 28 rue du Docteur Roux, F-75015 Paris, France.

[6]Department of Physics, Wellesley College, 106 Central Street, Wellesley, Massachusetts, 02481, United States.

[7]Trinity Centre for Bioengineering, Trinity Biomedical Sciences Institute, Trinity College Dublin, Dublin 2, D02 R590, Ireland.

*correspondence to: voneuws@tcd.ie; falko@marine.rutgers.edu

Abstract:

Materials science has been informed by nonclassical pathways to crystallization based on biological processes to fabricate damage-tolerant composite materials. Various biomineralizing taxa, such as stony corals, deposit metastable, magnesium-rich, amorphous calcium carbonate nanoparticles that further assemble and transform into higher-order mineral structures. Here we examine a similar process in abiogenic conditions using synthetic, amorphous calcium magnesium carbonate nanoparticles. Applying a combination of high-resolution imaging and *in situ* solid-state nuclear magnetic resonance spectroscopy, we reveal the underlying mechanism of the solid-state phase transformation of these amorphous nanoparticles into crystals under aqueous conditions. These amorphous nanoparticles are covered by a hydration shell of bound water molecules. Fast chemical exchanges occur: the hydrogens present within the nanoparticles exchange with the hydrogens from the surface-bound H_2O molecules which, in turn, exchange with the hydrogens of the free H_2O molecule of the surrounding aqueous medium. This cascade of chemical exchanges is associated with an enhanced mobility of the ions/molecules that compose the nanoparticles which, in turn, allow for their rearrangement into crystalline domains via solid-state transformation. Concurrently, the starting amorphous nanoparticles aggregate, and form ordered mineral structures through crystal growth by particle attachment. Sphere-like aggregates and spindle-shaped structures were respectively formed from relatively high or low weights per volume of the same starting amorphous nanoparticles. These results offer promising prospects for exerting control over such a non-classical pathway to crystallization to design mineral structures that could not be achieved through classical ion-by-ion growth.

Main text:

Exerting control over non-classical pathways to crystallization to direct the growth, polymorphism, and self-assembly of inorganic nanoparticles into higher-order structures is an important goal of materials sciences, writ large [1–9]. To achieve this, the dominant strategy is to govern the initial nucleation stage in a multitude of precipitation reactions occurring far from thermodynamic equilibrium [10]. These reactions share the common purpose of converting solution precursors into solid mineral materials [11] and use various approaches to overcome the free-energy barrier to nucleation. In the case of calcium carbonate and calcium phosphate minerals, these approaches were initially implemented to uncover the biomineralization processes being used by marine calcifiers and vertebrates to allow support [12], mastication [13], defense [14], attack [15], or optical [16] functions. They span from the utilization of (i) supersaturated concentrations [17–19] sometimes combined with (ii) confinement effects [20–23], the use of (iii) templates for epitaxial growth [24], and of (iv) various types of mineralization-directing agents such as synthetic polyelectrolytes [25–29], proteins [30–34] and amino acids [35–37]. The future exploitation of stable pre-nucleation clusters [38–40] may offer additional prospects for exerting some control over various non-classical crystallization processes [41,42].

Some of the above mentioned approaches were successfully applied to design and manufacture different nature-inspired inorganic-organic composite materials [43–48]; however, they suffer from two main limitations. First, they often lead to final materials which are very limited in terms of size (generally not exceeding a few millimeters along one dimension). Second, the level of mineralization does not reach those of their natural analogues, principally bone and nacre. The latter is the main limitation that prevents the fabrication of high strength materials. Here we consider an alternative strategy that overcome these limitations and allow the manufacturing of novel materials. Future approaches likely will skip over the initial nucleation stage on which little control can be exercised, and focus on the conversion of solid,

71 metastable amorphous nanoparticles into their crystalline counterparts. Such metastable

72 amorphous nanoparticles that assemble and transform into higher-order, hierarchical mineral

73 structures have been observed across various biomineralizing taxa [49–59], but their use in

74 synthetic systems remains extremely limited [60–64]. Here we used Amorphous Calcium

75 Magnesium Carbonate (ACMC) nanoparticles as models since most biogenic deposits of

76 amorphous $CaCO_3$ contain Mg^{2+} ions [49,65,66]. Especially, we monitored their pathway to

77 crystallization in wet conditions to understand their potential use in the development of novel

78 materials. To this end, we applied a combination of high-resolution imaging and *in situ* solid-

79 state nuclear magnetic resonance (NMR) spectroscopy. In particular, the latter technique

80 provides unprecedented atomic-scale insights into the mechanism of phase transformation of

81 these amorphous nanoparticles over time.

82 **Chemical structure and composition**

83 A number of physical characterization techniques were applied to assess the structure

84 and composition of a ^{13}C-labelled (98 atom% ^{13}C) Amorphous Calcium Magnesium

85 Carbonate (ACMC) sample. This sample was first studied in dry conditions. Powder X-ray

86 diffraction observations confirm that this is a non-crystalline solid given the absence of Bragg

87 reflections (**Fig. S1**). According to TGA measurements (**Fig. S2**), the mass fraction of the

88 hydrous species associated with the particles of ACMC is in the range of 22 to 26 wt. %. An

89 average atomic Ca/Mg ratio ≈ 4.0 was estimated using energy-dispersive X-ray spectroscopy

90 (EDS). As such, the atom% of Mg in ACMC [defined as Mg/(Ca + Mg) x 100] is about 20.0.

91 This is similar to the value found in a number of biogenic deposits of amorphous calcium

92 carbonate such as those in the cuticles and gastroliths in crustaceans, along with those in the

93 spicules in cnidarians [65]. Scanning Helium Ion Microscopy (SHIM) observations show that

94 ACMC is in the form of spherical nanosized particles with a diameter of about 60 to 90 nm

95   (**Fig. 1A**). These features resemble those of biogenic, magnesium-rich, amorphous calcium

96   carbonate particles present at early stages of coral biomineralization (**Fig. 1B**).

97   Solid-state Nuclear Magnetic Resonance (ssNMR) spectroscopy was applied to

98   investigate the carbon and hydrogen chemical environments of ACMC. One dimensional (1D)

99     $\{^1H\}^{13}C$ cross polarization (CP) (solid lines), and ^{13}C single-pulse (SP) (doted lines) magic

100   angle spinning (MAS) ssNMR spectra of ACMC are shown in **Fig. S3**. Both spectra are in the

101   form of a single, symmetric resonance whose carbon chemical shift [$\delta(^{13}C)$ = 168.2 ppm], full

102   width at half maximum (FWHM = 3.9 ppm) and Gaussian lineshape are characteristic of

103   carbonate ions (CO_3^{2-}) present in amorphous environments. This carbon chemical shift is

104   similar with that of calcite [67] which suggests that the present sample may be considered as a

105   proto-calcite amorphous calcium carbonate [68]. Further, the resonance in the ^{13}C SP spectrum

106   is identical with the one in the $\{^1H\}^{13}C$ CP spectrum in terms of lineshape and linewidth:

107     $\delta(^{13}C)$ = 168.2 ppm and full FWHM = 3.9 ppm. This statement stands true regardless the CP

108   contact time (t_{CP}) as shown in **Fig. S4** where t_{CP} was varied from 0.2 to 10 ms. The $\{^1H\}^{13}C$

109   CP spectrum selectively exposes ^{13}C nuclei nearby ^1H nuclei that belong to different rigid

110   hydrogen-bearing ions/molecules, whereas the ^{13}C SP spectrum reveals all ^{13}C nuclei since it

111   was recorded in quantitative conditions. Indeed, a long relaxation delay (RD) of 600 seconds

112   was chosen to allow for full relaxation of the longitudinal magnetization. According to their

113   similarity in terms of lineshape and linewidth, the $\{^1H\}^{13}C$ CP spectrum exposes similar ^{13}C

114   nuclei as those observed upon direct excitation in the quantitative ^{13}C SP spectrum. These

115   observations provide important structural and chemical information. First, this is evidence that

116   the rigid hydrogen-bearing ions/molecules are homogenously distributed throughout the

117   amorphous calcium carbonate nanoparticles; and a similar conclusion was previously reached

118   by others [68,69]. Second, this also rules out the presence of bicarbonate ions (HCO_3^-) given the

119   absence of a distinct upfield signal at short contact time (expected in the range of $\delta(^{13}C) \approx$

120   155-165 ppm [67,70,71]).

121   To reveal the nature of the hydrogen-bearing ions/molecules present in the amorphous

122   nanoparticles, further ^1H-based ssNMR experiments were applied. The 1D ^1H direct

123   excitation (DE) MAS ssNMR spectrum of ACMC is shown in **Fig. S5A**. However, this

124   spectrum exposes a broad signal centered around $\delta(^1H) = 4.9$ ppm along with two narrow

125   resonances at $\delta(^1H) = 1.2$ and 3.6 ppm respectively, respectively due to the presence of water

126   and mobile ethanol molecules weakly adsorbed onto the surface of the particles. The latter

127   originate from anhydrous ethanol that was used post-precipitation to allow preservation of the

128   solid as an amorphous phase upon storage. As an alternative, we recorded a 1D $\{^1H-^{13}C\}^1H$

129   double cross polarization (CP) MAS ssNMR experiment (**Fig. S5B**). It gives rise to a ^{13}C-

130   filtered ^1H spectrum whose signals correspond to structural hydrogen-bearing ions/molecules

131   present within the amorphous nanoparticles. This approach was successfully used to

132   investigate the hydrogen-bearing ions/molecules present in bone mineral in intact bone tissue

133   [72]. Here two main resonances are clearly observable. According to their respective chemical

134   shift, they reflect the presence of hydroxyl ions (OH^-) [observable at $\delta(^1H) = 1.0$ ppm [73,74]]

135   and structural water molecules [observable at $\delta(^1H) = 5.6$ ppm]. In addition, the apparent

136   dissymmetry of the main water resonance suggests the presence of a broad downfield signal

137   that spreads up to $\delta(^1H) \approx 13$ ppm (black arrow). Further, the fact that the ^{13}C-filtered ^1H

138   spectrum cannot be satisfactory fitted with only two peaks at $\delta(^1H) = 1.0$ ppm (OH^-) and 5.6

139   ppm (H_2O) confirms the presence of this additional broad signal (**Fig. S6A**). In contrast, the

140   same ^{13}C-filtered ^1H spectrum can be properly fitted with three peaks at $\delta(^1H) = 1.0$ ppm (OH^-

141   ), 5.6 ppm (H_2O) and 7.0 ppm (**Fig. S6B**). The use of a single peak centered at $\delta(^1H) = 7.0$

142   ppm to materialize the additional broad signal is somewhat arbitrary. Indeed, this broad signal

143   is probably composed of heterogeneous hydrogen environments leading to a wide distribution

144 of NMR chemical shifts. However, the fact that this broad signal is centered at $\delta(^1H) = 7.0$

145 ppm suggests the presence of structural water molecules engaged in stronger hydrogen bonds

146 than those observed at $\delta(^1H) = 5.6$ ppm [75].

Kinetics of crystallization

148 Time resolved, *in situ* ssNMR experiments were undertaken to investigate the kinetics

149 of crystallization of ACMC under aqueous conditions. To this end, the amorphous powder

150 was soaked in deionized water. Following this, 1D ^{13}C single-pulse (SP) MAS ssNMR spectra

151 were recorded consecutively. After a period of approximately 1 h, a second carbon resonance

152 appears, and its intensity increases over time (**Fig. 2A**). This second carbon resonance is

153 narrow (FWHM = 0.70 ppm) and centered at $\delta(^{13}C) = 171.7$ ppm, and, hence, reflects the

154 growth of monohydrocalcite (MHC, calcium carbonate monohydrate: $CaCO_3.H_2O$) [67].

155 Monohydrocalcite is one of the six crystalline forms of calcium carbonate. It is deposited in a

156 variety of sedimentary environments (*e.g.*, lakes [76] and speleothems [77]). Monohydrocalcite is

157 also the result of a number of biomineralization processes including otoliths of vertebrates [78],

158 calcareous corpuscles of certain flatworms [79] and guinea pig bladder stones [80]. Further,

159 monohydrocalcite could also be a metastable intermediate phase in the formation of both

160 aragonite and calcite [81,82]. It is well documented that amorphous calcium carbonates are

161 metastable and spontaneously crystallize in water. Especially if crystallization occurs via

162 solid-state transformation (which is discussed in the next section), one could expect here the

163 formation of calcite since ACMC may be considered as a proto-calcite amorphous calcium

164 carbonate (**Fig. S3**). However, it is also well documented that magnesium regulates the

165 crystallization of amorphous calcium carbonates [83,84] and, in certain conditions, favors the

166 formation of monohydrocalcite [81,82,85–87]. Here the consecutive ^{13}C SP MAS ssNMR spectra

167 were recorded under quantitative conditions (recycling delay, RD = 600s). As such, they

168 allow for determining the conversion rate of the starting amorphous environments into

7

169   monohydrocalcite as a function of time (**Fig. 2B**). This conversion rate is here expressed in

170   terms of the molar percentage of carbonate ions present in monohydrocalcite environments.

171   To achieve this, the consecutive ^{13}C SP MAS ssNMR spectra were all fitted with two peaks as

172   shown in **Fig. S7**. The area under each peak was integrated to obtain the molar ratio of

173   carbonate ions present in crystalline and amorphous environments. As a result, here we show

174   that nearly 40% of the carbonate ions of ACMC were converted into monohydrocalcite after a

175   period of about 20 h.

176   **Solid-state phase transformation versus dissolution-reprecipitation?**

177   To shed light on the phase transformation process of ACMC into monohydrocalcite, a

178   two-dimensional (2D) ^{13}C-^{13}C Dipolar Assisted Rotational Resonance (DARR) MAS ssNMR

179   experiment was performed (**Fig. 3A**). To this end, the amorphous powder was soaked in water

180   until its conversion rate into monohydrocalcite reached about 30%, which took approximately

181   12 h (**Fig. 2B**). The 2D ^{13}C-^{13}C DARR MAS ssNMR spectrum is in the form of a ^{13}C-^{13}C

182   correlation map in which off-diagonal signals are due to magnetization exchange between

183   nearby ^{13}C nuclei. Here a strong off-diagonal signal (red dotted lines) connects the carbonate

184   ions present in monohydrocalcite [observable at $\delta(^{13}C) = 171.7$ ppm] with those present in the

185   amorphous environments [observable at $\delta(^{13}C) = 168.2$ ppm]. As a consequence, these results

186   clearly suggest that the nascent crystalline environments together with the starting amorphous

187   environments belong to the same particles. This is strong evidence that the starting amorphous

188   nanoparticles transform into monohydrocalcite via a mechanism of solid-state phase

189   transformation.

190   An alternative scenario would see first the dissolution of the starting amorphous

191   nanoparticles followed by their reprecipitation into monohydrocalcite. Indeed, using various

192   methods [including isotopic labelling [88], in situ liquid cell transmission electron microscopy

193   (TEM) [89] and Raman spectroscopy [82], time resolved scanning electron microscopy (SEM) [86],

194   pH and supersaturation measurements [90], Energy Dispersive X-ray Diffraction (ED-XRD) [91],

195   small and wide angle X-ray scattering (SAXS/WAXS) [81,92], or the combination of several of

196   these techniques], various mechanisms including steps of dissolution-reprecipitation were

197   pointed out in the pathway to crystallization of different nanoparticles of synthetic amorphous

198   calcium carbonates into calcite, magnesian calcite, aragonite, vaterite and even

199   monohydrocalcite. Why under certain conditions some types of nanoparticles of amorphous

200   calcium carbonate crystalize via solid-state transformation while some others first dissolve

201   and then reprecipitate is still unclear. This major discrepancy is certainly multifactorial,

202   depending on the polymorph and the chemical composition of the starting amorphous

203   particles together the chemistry of the reaction solution. In this direction, a recent study

204   suggests that the presence of Mg^{2+} ions incorporated in the solid phase brings excess

205   structural water which, in turn, "weakens the ionic binding network" and favors a solid-state

206   transformation [89]. In addition, it was also reported that an increased water content accelerates

207   the mechanism of solid-state transformation in the case of a temperature-induced

208   crystallization [93,94]. As such, it is important to rule out the eventuality of a mechanism of

209   dissolution-reprecipitation during the crystallization of ACMC in the present study. To this

210   end, we simulated a mechanism of dissolution-reprecipitation using a physical mixture

211   containing 40 wt. % monohydrocalcite particles and 60 wt. % amorphous particles soaked in

212   water. The former particles originate from a new ^{13}C-labelled (99 atom% ^{13}C)

213   monohydrocalcite sample (MHC) (whose powder X-ray diffraction pattern is shown in **Fig.**

214   **S8**) that was prepared by a direct precipitation method [85], whereas the latter particles are those

215   of the amorphous ACMC sample. The ^{13}C-^{13}C DARR MAS ssNMR spectrum of this physical

216   mixture soaked in water is shown in **Fig. 3B**. This spectrum was recorded within 90 minutes

217   following the wetting step so that the conversion rate of ACMC into monohydrocalcite

218   remains very low (must be below ≈ 2% - **Fig. 2B**). As expected, here the absence of off-

219 diagonal signal confirms that the carbonate ions present in the monohydrocalcite

220 environments of MHC are not in proximity with those present in the amorphous environments

221 of ACMC. As such, the observation of an off-diagonal signal in the ^{13}C-^{13}C DARR MAS

222 ssNMR spectrum of the ACMC sample partially converted into monohydrocalcite excludes a

223 mechanism of dissolution-reprecipitation (**Fig. 3A**).

Surface hydration shell and Hydrogen-Hydrogen chemical exchanges

225 The possible interactions of the amorphous nanoparticles of ACMC with water

226 molecules were examined. To this end, 2D {^{1}H}^{13}C HetCor MAS ssNMR experiments of

227 ACMC were performed both in dry and wet conditions (**Fig. 4)**. In wet conditions, the sample

228 was soaked in water and the 2D {^{1}H}^{13}C HetCor MAS ssNMR experiment was performed

229 within one hour following the wetting step. In these conditions, monohydrocalcite has yet not

230 been formed, or rather remains below the detection threshold of ssNMR (**Fig. 2B**). These 2D

231 {^{1}H}^{13}C HetCor MAS ssNMR spectra are in the form of ^{1}H-^{13}C correlation maps in which the

232 different signals, named "correlation peaks", reveal atomic-scale spatial proximities among

233 rigid hydrogen-bearing ions/molecules (displayed along the vertical, indirect ^{1}H dimension)

234 and carbon-bearing ions (displayed along the horizontal, direct ^{13}C dimension). In dry

235 conditions, a broad signal associated with two intense spinning sidebands are observable. This

236 signal results from the juxtaposition of two different correlation peaks which, similarly to the

237 {^{1}H-^{13}C}^{1}H double cross polarization (CP) MAS ssNMR experiment, are due to the presence

238 of OH^{-} ions [observable at $\delta(^{1}\text{H}) \approx 1.0$ ppm] and structural water molecules [observable in the

239 range of $\delta(^{1}\text{H}) \approx 5\text{-}13$ ppm]. In contrast, in wet conditions, only a single and sharp correlation

240 peak is observable while the two intense spinning sidebands are no longer observable. This

241 sharp correlation peak is at $\delta(^{1}\text{H}) = 4.7$ ppm (FWHM = 0.6 ppm) in the indirect ^{1}H dimension,

242 and, hence, reflects the presence of water molecules. Since Brownian motion averages dipolar

243 couplings to zero, these water molecules must be adsorbed onto the particles' surface to allow

244   CP magnetization transfer. We can infer from this that a hydration shell of bound water forms

245   around the particles of ACMC under aqueous conditions.

246   Further, the fact that the broad isotropic signal seen in dry conditions is no longer

247   observed in wet conditions where only a sharp water correlation peak is present (**Fig. 4**), is

248   diagnostic of a fast hydrogen exchange regime on the NMR time scale. Indeed, this is

249   evidence that fast chemical exchanges occur between hydrogens from the free water

250   molecules and those from the rigid hydrogen-bearing ions/molecules (i.e., OH^- and H_2O)

251   present in the amorphous solid. Due to the presence of the hydration shell of bound water,

252   these chemical exchanges are likely to occur in two steps: the hydrogens present in the

253   amorphous solid phase exchange with the hydrogens from the surface-bound H_2O molecules

254   which, in turn, exchange with the hydrogens of the free H_2O molecule of the surrounding

255   aqueous medium. Our TGA measurements (**Fig. S2**) show that, in dry conditions, the mass

256   fraction of the different populations of hydrogen-bearing ions/molecules (OH^- and H_2O)

257   associated with the particles of ACMC is in the range of 22 to 26 wt. %. As a result, we could

258   calculate the proportion of hydrogens originating from the particles over the total number of

259   hydrogens present in the MAS rotor following the wetting step: i.e., from about 5 to 10%. The

260   number of hydrogens from the free water molecules is therefore in large excess over the

261   number of hydrogens present in the particles and, hence, the latter are not detected in wet

262   conditions (fast exchange regime) and solely the excess water signal is observed at $\delta(^1H) =$

263   4.7 ppm. In addition, the fact that the two intense spinning sidebands observed in dry

264   conditions are no longer observable when the particles are soaked in water also advocate for

265   chemical exchanges. This is evidence that the hydrogens from the particles were mobilized in

266   wet conditions due to their exchanges with the hydrogens from the free water molecules.

267   Further, similar hydrogen-hydrogen exchanges were also pointed out not only for synthetic

268 particles of amorphous calcium phosphate (ACP) soaked in water, but also for the ACP-like

269 surface of bone mineral particles from a fresh and intact bone tissue sample [95].

270   For further evidence of the presence of a hydration shell of bound water, cryogenic

271 transmission electron microscopy (cryo-TEM) observations were obtained from the

272 amorphous nanoparticles of ACMC dispersed in water (**Fig. S9**). This dispersion was

273 cryofixed in liquid ethane within 10 min after its preparation and, hence, crystallization has

274 not yet started. A low magnification micrograph shows aggregates of nanoparticles that were

275 highlighted by yellow circles in **Fig. S9A**. Regions immediately around these aggregates

276 appear darker, indicating that the amorphous ice is thicker. This is evidence that the

277 nanoparticles (shown at higher magnification in **Fig. S9B)** retain water. Further, when these

278 nanoparticles are not "piled up" on top of each other as those pointed out with yellow arrows

279 in **Fig. S9B**, tiny lighter zones are visible and are certainly due to the presence of pores.

280 These pores are almost certainly not artifacts caused by electron beam irradiation since they

281 do not evolve upon prolonged observation. As a result, we suggest that the pores facilitate the

282 fast hydrogen-hydrogen exchanges that we observed in the 2D $\{^1H\}^{13}C$ MAS HetCor ssNMR

283 experiments performed in wet conditions.

284   To better understand the origin of the hydrophilic properties of ACMC, we examined

285 whether a surface hydration shell can also form around the particles of a hydrated calcium

286 carbonate mineral soaked in water. To this end, the MHC sample was used since

287 monohydrocalcite ($CaCO_3.H_2O$, with one water molecule per calcium carbonate group) is a

288 suitable model mineral for amorphous calcium carbonates in terms of chemical composition

289 [96]. The ^{13}C single-pulse (SP) MAS ssNMR spectrum of MHC is shown in **Fig. S10A**. This

290 sample is mainly composed of monohydrocalcite environments, but also contains residual

291 amorphous environments that were not converted into monohydrocalcite (**Fig. S10B**). Further,

292 the 1D $\{^1H-^{13}C\}^1H$ double cross polarization (CP) MAS ssNMR spectrum of MHC is shown

293   in **Fig. S10C**. This spectrum exposes a single, symmetric resonance [centered at $\delta(^1H) = 6.0$

294   ppm; FWHM = 8.9 ppm] attributed to structural water molecules in monohydrocalcite

295   environments. As for the possible interactions of the particles of MHC with water molecules,

296   they were investigated in a similar manner as for ACMC. Two-dimensional $\{^1H\}^{13}C$ HetCor

297   MAS ssNMR experiments of MHC were performed both in dry and wet conditions and are

298   shown in **Fig S11**. The signal due to the presence of the residual amorphous environments

299   differs in dry and wet conditions. While this signal is broad and barely visible is dry

300   conditions (grey arrow), it is clearly detected in wet conditions where a sharp correlation peak

301   at $\delta(^1H) = 4.7$ ppm in the indirect ^1H dimension shows the presence of surface-bound water

302   molecules. In contrast, the signal due to the presence of the monohydrocalcite environments

303   was unchanged after hydration. In both dry and wet conditions, this signal is in the form of a

304   broad correlation peak due to the presence of CO_3^{2-} ions [observable at $\delta(^{13}C) = 171.7$ ppm in

305   the direct ^{13}C dimension] near structural H_2O molecules [centered at $\delta(^1H) = 6.0$ ppm in the

306   indirect ^1H dimension]. As such, contrary to the amorphous environments of MHC but also

307   those of ACMC, the presence of an excess of free water in the MAS rotor does not cause the

308   formation of a hydration shell of bound water associated with the monohydrocalcite

309   environments. These results suggest that the hydrophilic properties of ACMC are not due to a

310   specific chemical composition including Ca^{2+} and CO_3^{2-} ions along with structural H_2O

311   molecules, but are rather the result of a definite amorphous structure.

312   **Evolution of the hydrogen chemical environments as crystallization progresses**

313   The evolution of the hydrogen chemical environments during the conversion of the

314   starting amorphous nanoparticles into monohydrocalcite was also scrutinized. To this end,

315   additional 2D $\{^1H\}^{13}C$ HetCor MAS ssNMR experiments of ACMC soaked in water were

316   therefore undertaken consecutively following the initial wetting step (**Fig. 5**). The previously

317   mentioned, quantitative 1D ^{13}C SP MAS ssNMR spectra, were recorded between each of

318   these 2D {^{1}H}^{13}C HetCor experiments so that the molar percentage of monohydrocalcite is

319   known. Here the growth of monohydrocalcite appears in the form of a broad, composite

320   signal along the vertical, indirect ^{1}H dimension whose intensity progressively increases

321   [observable at $\delta(^{13}$C$) = 171.7$ ppm in the horizontal, direct ^{13}C dimension]. This broad,

322   composite signal is also observable in the ^{1}H slices taken at the monohydrocalcite position

323   (**Fig. S12A**). The signal arises from hydrogen-bearing ions/molecules present within the

324   nascent crystalline environments and spreads from $\delta(^1$H$) \approx$ -5 to 15 ppm; this is in agreement

325   with the ^{13}C-filtered ^{1}H MAS NMR spectrum of the reference sample of monohydrocalcite

326   shown in **Fig. S10C**. Moreover, intense spinning sidebands, signature of hydrogen-bearing

327   ions/molecules with restricted mobility, are also observed in agreement with the crystalline

328   nature of these nascent environments (**Fig. S12A**).

329   As for the starting amorphous environments, a sharp water correlation peak not

330   associated with any spinning sidebands (which is diagnostic of a fast hydrogen exchange

331   regime on the NMR time scale) is visible at the ACMC position [i.e., $\delta(^{13}$C$) = 168.2$ ppm in

332   the horizontal, direct ^{13}C dimension] (**Fig. 5**). As a result, the ^{1}H slices taken at the ACMC

333   position only expose a single and narrow resonance [centered at $\delta(^1$H$) = 4.7$ ppm; FWHM in

334   the range of 0.6 to 1.3 ppm] attributed to water molecules bound to the particles' surface (**Fig.**

335   **S12B**). These observations are similar to what is observed for ACMC in wet conditions before

336   crystallization (**Fig. 4B**), and highlight that the starting amorphous environments remain

337   hydrated while crystallization progresses. They also imply that the hydrogen-bearing

338   ions/molecules remaining in the starting amorphous environments keep undergoing chemical

339   exchanges with the free water molecules as crystallization progresses.

340   **Hydrogen-deuterium chemical exchanges**

341   For further evidence of these chemical exchanges, 2D {^{1}H}^{13}C HetCor MAS ssNMR

342   experiments of ACMC soaked in heavy water (D$_2$O - 99.99 atom% D) were undertaken

343 sequentially (**Fig. 6**). Quantitative 1D ^{13}C SP MAS ssNMR spectra were recorded between

344 each of the 2D {^{1}H}^{13}C HetCor experiments so that the conversion rate of ACMC into

345 monohydrocalcite is known. Here this conversion rate reaches up 26% after 1130 minutes

346 which is therefore about 40% lower than in the case of ACMC soaked in H_2O at the same

347 stage (conversion rate, 36%) (**Fig. 2B**); and this discrepancy is likely related to a kinetic

348 isotope effect. In contrast to the successive 2D {^{1}H}^{13}C HetCor MAS ssNMR spectra of

349 ACMC soaked in H_2O where a broad, composite signal was observed along the indirect ^{1}H

350 dimension, here the growth of monohydrocalcite appears in the form of a single, narrow

351 correlation peak [observable at $\delta(^{13}C) = 171.7$ ppm in the horizontal, direct ^{13}C dimension].

352 The ^{1}H slices taken at the monohydrocalcite position reveal a single, symmetric resonance

353 [centered at $\delta(^1H) = 6.0$ ppm; FWHM = 2.2 ppm] (**Fig. S13A**); this chemical shift is

354 characteristic of structural water molecules in monohydrocalcite environments (**Fig. S10C**).

355 However, the associated linewidth is much smaller due to a reduction of the ^{1}H dipolar

356 couplings induced by a partial deuteration. Indeed, here ^{1}H/^{2}H chemical exchanges led to the

357 deuteration of the hydrogen-bearing ions/molecules present in the starting amorphous

358 nanoparticles before crystallization occurs (after about 1 h - **Fig. 2B**). As a result, the protium

359 isotopes, originating from ACMC, were diluted following the addition of the large excess of

360 deuterium isotopes originating from the D_2O solution [^{2}H/(^{2}H + ^{1}H) $\geq$ 90 atom% in the MAS

361 rotor]. This "isotopic dilution" has largely lowered the magnitude of the homonuclear ^{1}H-^{1}H

362 dipolar couplings within the particles which, in turn, gave rise to ^{1}H spectra of the

363 monohydrocalcite environments with higher resolution (compared with H_2O). The same

364 phenomenon also explains the presence of weaker spinning sidebands associated with the

365 nascent crystalline environments growing in D2O compared to H_2O (**Fig. S13A**).

366 As for the starting amorphous environments, the sharp water correlation peak that was

367 previously seen at $\delta(^1H) = 4.7$ ppm (FWHM in the range of 0.6 to 1.3 ppm) along the indirect

368 ^{1}H dimension of the successive 2D {^{1}H}^{13}C HetCor MAS ssNMR spectra of ACMC soaked

369 in H_2O was not observed. Instead, two narrow correlation peaks due to the presence of

370 structural OH^- ions [$\delta(^1H)$ = 1.0 ppm - no longer observed after 330 min] and structural water

371 molecules [$\delta(^1H)$ = 5.6 ppm; FWHM $\approx$ 2.9 ppm] arise from the starting amorphous

372 environments (**Fig. 6**). The intensity of the water correlation peak progressively declines up to

373 970 minutes, after which the peak becomes almost no longer visible; this is also observable in

374 the ^{1}H slices taken at the ACMC position [i.e., $\delta(^{13}C)$ = 168.2 ppm in the direct ^{13}C

375 dimension] (**Fig. S13B**). The number of hydrogens originating from the particles initially

376 represents almost 100% of the total number of hydrogens present in the MAS rotor following

377 the wetting step with D_2O. The surface-bound water molecules (mostly in the form of D_2O,

378 and in a less extent H_2O but also HDO that were formed following the chemical exchanges)

379 are not detected in the 2D {^{1}H}^{13}C HetCor spectra due to the fast exchange regime where

380 solely the excess OH^- / H_2O and HDO signals arising from the particles are observed. Further.

381 the disappearance of these OH^-/ H_2O and HDO signals is due to the rearrangement of these

382 populations of hydrogen-bearing ions/molecules present in the starting amorphous

383 environments to form of monohydrocalcite via a solid-state phase transformation (**Fig. 3A**).

384 **Crystal growth by accretion of amorphous nanoparticles**

385 The mineral structures resulting from the crystallization of ACMC soaking in water in

386 the MAS rotor were scrutinized by Scanning Helium Ion Microscopy (SHIM). To this end,

387 the previously mentioned, consecutive ^{13}C SP MAS ssNMR experiments of ACMC soaked in

388 water, have been run until the signal arising from the starting amorphous environments stops

389 evolving (after a period of approximately 2500 min). Hence, at this stage, the conversion rate

390 of ACMC into monohydrocalcite has reached its maximum (**Fig. S14**). Following this, the

391 wet powder was simply collected from the MAS rotor, washed with deionized water, and then

392 dried at ambient temperature. The resulting dry powder was analyzed by X-ray diffraction

16

393   that has confirmed the presence of monohydrocalcite (**Fig S15**). From the same powder, an

394   average atomic Ca/Mg ratio ≈ 5.0 was estimated using energy-dispersive X-ray spectroscopy

395   (EDS). It corresponds to an atom% of Mg in ACMC converted into monohydrocalcite

396   [defined as Mg/(Ca + Mg) x 100] of about 16.6 (against 20.0 for ACMC before

397   crystallization). It shows that a small proportion of Mg^{2+} have been expelled out of the

398   particles following crystallization. This suggests that the leading process of solid-state

399   transformation of ACMC into monohydrocalcite is here associated with a small loss of

400   magnesium that possibly occurs via a mechanism of Ostwald ripening [81]. As for the SHIM

401   observations, a low magnification micrograph clearly shows that the crystallization process of

402   ACMC occurs via a spherulitic growth mechanism (**Fig. 7A**). Successive magnification

403   micrographs on an open spherulite reveal the presence of crystals that greatly differ from the

404   classical view of inorganic crystals with faceted surfaces (**Fig. 7, B to D**). Instead, acicular

405   crystals displaying a highly textured surface due to the apparent presence of spherical

406   nanoparticles "building-blocks" are here observed. Similar acicular crystals are also

407   observable at the surface of a spherulite (double yellow arrows in **Fig. 7E**), where the

408   spherical nanoparticles "building-blocks" match with the starting amorphous nanoparticles of

409   ACMC in terms of size (**Fig. 7F**). Such "nano-particulate" texture was initially observed for

410   biological aragonite in nacre [53,97] and more recently for biological aragonite in coral (**Fig. 7G**)

411   [49] and across a broad range of biomineralizing taxa [98]. This "nano-particulate" texture is

412   another evidence for a mechanism of solid-state transformation; this is also signature of

413   crystal growth by accretion of amorphous nanoparticles [99,100] which is one variety of

414   crystallization by particle attachment [101].

415   In addition, in order to assess the behavior of ACMC within in a higher volume of

416   water, the mineral structures resulting from the crystallization of ACMC soaking in a reaction

417   vial instead of in an NMR rotor were also scrutinized. To this end, the amorphous

418 nanoparticles of ACMC were dispersed in deionized water in a 10ml vial (mass concentration

419 ≈ 2% w/v against about 30% w/v in the MAS rotor) and the resulting suspension was aged for

420 a period of 24 hours to allow crystallization. This dispersion was then cryofixed in liquid

421 ethane and imaged using cryogenic transmission electron microscopy (cryo-TEM). In the

422 present conditions, sphere-like aggregates were not observed but a low magnification

423 micrograph instead shows the presence of spindle-shaped, higher-order mineral structures

424 (**Fig. S9C**). These mineral structures have a length from 800 to 1700 nm and a thickness from

425 200 to 500 nm. At high magnification, it is clear that they are not monolithic but are rather in

426 the form of bundles of smaller parallel units (**Figs. 7H and S9D**). Selected-area electron-

427 diffraction (SAED) shows that these bundles of smaller parallel units are composed of

428 monohydrocalcite (inset in **Fig. 7H**). Similar spindle-shaped mineral structures were also

429 observed following the crystallization of amorphous calcium carbonate nanoparticles into

430 aragonite [102]. In this study, nanoscale crystals formed within an "amorphous framework"

431 composed of aggregated amorphous nanoparticles. Our results support an analogous

432 mechanism for the crystallization of ACMC into monohydrocalcite: the amorphous

433 nanoparticles first aggregate (**Fig. S9A**) and then crystalize via solid-state transformation

434 (**Figs. 3A, 7H and S9B**).

435 **Chemical and structural model of the surface region**

436 The results presented in the present study allowed us to design a two-dimensional

437 chemical and structural model of the surface region of an amorphous particle of ACMC

438 soaked in water (**Fig. 8B**). The amorphous solid phase (grey area) is composed of

439 homogeneously distributed, structural OH^- ions and H_2O molecules close to CO_3^{2-} ions. Here

440 the coordination number of the cations is arbitrary. But a ^{25}Mg-based solid-state NMR study

441 suggests that, in Mg-stabilized amorphous calcium carbonates, each Mg^{2+} are surrounded by

442 4-4.5 CO_3^{2-} ions in average along with at least one H_2O molecule [103]. The surface of the

443   nanoparticle is hydrophilic and, hence, they are covered by a hydration shell of bound water.

444   The assumption was made that the water molecules of the hydration shell form a second

445   sphere of coordination around the surface ions. Fast chemical exchanges continuously occur:

446   the hydrogens present in the amorphous solid phase exchange with the hydrogens from the

447   surface-bound H_2O molecules which, in turn, exchange with the hydrogens of the free H_2O

448   molecule of the surrounding aqueous medium. These exchanges may be facilitated due to the

449   presence of pores (size, 1 to 3 nm) seen in the cryo-TEM micrograph shown in **Fig. 8A**.

450   **Conclusions**

451   Our results reveal the underlying mechanism of the solid-state phase transformation of

452   Amorphous Calcium Magnesium Carbonate (ACMC) nanoparticles into crystals under

453   aqueous conditions. First, we showed that the ^{13}C-^{13}C Dipolar Assisted Rotational Resonance

454   (DARR) ssNMR technique can be used to assess whether crystallization occurs via

455   dissolution-reprecipitation or whether it occurs via solid-state transformation. Using this

456   technique, we show that the nascent crystalline environments in the form of monohyrocalcite

457   (MHC), together with the starting amorphous environments, belong to the same particles. This

458   is clear evidence of a solid-state phase transformation of the starting amorphous nanoparticles

459   into crystals. Second, we show that the surface of these amorphous nanoparticle is

460   hydrophilic. Indeed, when soaked in aqueous medium, these nanoparticles are covered by a

461   hydration shell of bound water (**Fig. 8**). As a result, when the particles come into contact

462   following aggregation or simple sedimentation, this hydration shell drives particle-particle

463   interactions. In a bigger picture, it is now acknowledged that "the role of hydration layers in

464   biogenic systems needs to be considered and may be responsible for phenomena seen in

465   biomineralization" [104]. Our results also show that fast chemical exchanges continuously occur:

466   the hydrogens present in the particles exchange with the hydrogens from the hydration shell

467   of bound water which, in turn, exchange with the hydrogens of the free H_2O molecule of the

468   surrounding aqueous medium. We also revealed that the starting amorphous nanoparticles

469   remain hydrated while crystallization progresses. And while the nanoparticles are partially

470   converted into monohydrocalcite, the domains part of the nanoparticles that remain

471   amorphous keep undergoing fast hydrogen-hydrogen chemical exchanges with the free H_2O

472   molecules of the surrounding aqueous medium. Hence, our results question the role played by

473   these unceasing chemical exchanges towards crystallization. While hydrogens from the

474   amorphous nanoparticles are relocated into the surrounding aqueous medium, hydrogens from

475   the aqueous medium travel the reverse path. As a result, H-bonds, that presumably stabilizes

476   amorphous solids against crystallization [105], are being constantly broken and reformed

477   throughout the amorphous solid. Our results suggest that this process is associated with an

478   enhanced mobility of the ions/molecules that compose the amorphous nanoparticles which, in

479   turn, could allow for rearrangement of these ions/molecules into crystalline domains via solid-

480   state transformation. Further, we can hypothesize what sometimes triggers the total

481   dissolution of certain amorphous nanoparticles under aqueous conditions [81,86] (not observed in

482   the present study). We presume that an increased content of structural hydrous species will

483   escalate the hydrogen-hydrogen exchanges and, concomitantly, rise the mobility of the

484   ions/molecules that compose the amorphous nanoparticles. This mobility could reach a certain

485   level where the amorphous nanoparticles breaks down into solubilized ions that are now

486   available to reprecipitate into a new solid phase. From a wider perspective, our results shed

487   light on the means available to living organisms for directing crystallization into a process of

488   solid-state transformation rather than one of dissolution-precipitation and, as such, could help

489   to reconstruct the puzzle of various biomineralization processes.

490   Last, the results presented here and elsewhere [89,102,106,107] reveal the capability of

491   synthetic, amorphous inorganic nanoparticles to form higher-order mineral structures through

492   pathways to crystallization that combine solid-state phase transformation and particle

493   attachment. As a such, taking advantage of these pathways to crystallization opens new

494   avenues in materials science based on future strategies that will no longer be limited by the

495   initial nucleation stage. In addition, since these pathways to crystallization also offers the

496   opportunity to shape the resulting higher-order mineral structures into different morphologies

497   [63] (such as the spherulitic aggregates and the spindle-shaped mineral structures shown in the

498   present study), they also pave the way for future strategies that will no longer be "restricted by

499   the constraints of the crystal unit cell" [4].

Supporting Information: X-ray diffraction analysis of ACMC (Figure S1); Weight

loss and heat flow measurements of ACMC (Figure S2); Carbon environments of ACMC

(Figure S3); Cross-polarization dynamics between ^1H and ^{13}C nuclei in ACMC (Figure S4);

Hydrogen environments of ACMC (Figure S5); Rigid hydrogen-bearing ions/molecules

present in ACMC (Figure S6); Evaluation of the conversion rate of ACMC into

monohydrocalcite (Figure S7); X-ray diffraction analysis of the monohydrocalcite sample

(Figure S8); Observations of the starting amorphous nanoparticles of ACMC and their

resulting higher-order mineral structures following crystallization (Figure S9); Carbon and

Hydrogen environments of the monohydrocalcite sample (Figure S10); Spatial proximities

among carbon-bearing ions and hydrogen-bearing ions/molecules in the particles of the

monohydrocalcite sample (Figure S11); Evolution of the hydrogen environments while the

amorphous nanoparticles of ACMC are crystalizing in water (Figure S12); Evolution of the

hydrogen environments while the amorphous nanoparticles of ACMC are crystalizing in

heavy water (Figure S13); Carbon environments of ACMC before and after crystallization

(Figure S14); X-ray diffraction analysis of ACMC following crystallization (Figure S15).

References

(1)   Cölfen, H.; Mann, S. Higher-Order Organization by Mesoscale Self-Assembly and Transformation of Hybrid Nanostructures. *Angew. Chem. Int. Ed.* **2003**, *42* (21), 2350–2365. https://doi.org/10.1002/anie.200200562.

(2)   Meldrum, F. C.; Cölfen, H. Controlling Mineral Morphologies and Structures in Biological and Synthetic Systems. *Chem. Rev.* **2008**, *108* (11), 4332–4432. https://doi.org/10.1021/cr8002856.

(3)   Imai, H. Mesostructured Crystals: Growth Processes and Features. *Prog. Cryst. Growth Charact. Mater.* **2016**, *62* (2), 212–226. https://doi.org/10.1016/j.pcrysgrow.2016.04.011.

(4)   Jehannin, M.; Rao, A.; Cölfen, H. New Horizons of Nonclassical Crystallization. *J. Am. Chem. Soc.* **2019**, *141* (26), 10120–10136. https://doi.org/10.1021/jacs.9b01883.

(5)   Rieger, J.; Kellermeier, M.; Nicoleau, L. Formation of Nanoparticles and Nanostructures-An Industrial Perspective on $CaCO_3$, Cement, and Polymers. *Angew. Chem. Int. Ed.* **2014**, n/a-n/a. https://doi.org/10.1002/anie.201402890.

(6)   Imai, H. Self-Organized Formation of Hierarchical Structures. In *Biomineralization I*; Naka, K., Ed.; Springer Berlin Heidelberg, 2007; Vol. 270, pp 43–72. https://doi.org/10.1007/128_054.

(7)   Cölfen, H.; Antonietti, M. Mesocrystals: Inorganic Superstructures Made by Highly Parallel Crystallization and Controlled Alignment. *Angew. Chem. Int. Ed.* **2005**, *44* (35), 5576–5591. https://doi.org/10.1002/anie.200500496.

(8)   Lee, J.; Yang, J.; Kwon, S. G.; Hyeon, T. Nonclassical Nucleation and Growth of Inorganic Nanoparticles. *Nat. Rev. Mater.* **2016**, *1* (8), 16034. https://doi.org/10.1038/natrevmats.2016.34.

(9)   Navrotsky, A. Energetic Clues to Pathways to Biomineralization: Precursors, Clusters, and Nanoparticles. *Proc. Natl. Acad. Sci.* **2004**, *101* (33), 12096–12101. https://doi.org/10.1073/pnas.0404778101.

(10)   Nakouzi, E.; Steinbock, O. Self-Organization in Precipitation Reactions Far from the Equilibrium. *Sci. Adv.* **2016**, *2* (8), e1601144. https://doi.org/10.1126/sciadv.1601144.

(11)   *New Perspectives on Mineral Nucleation and Growth*; Van Driessche, A. E. S., Kellermeier, M., Benning, L. G., Gebauer, D., Eds.; Springer International Publishing: Cham, 2017. https://doi.org/10.1007/978-3-319-45669-0.

(12)   Reznikov, N.; Bilton, M.; Lari, L.; Stevens, M. M.; Kröger, R. Fractal-like Hierarchical Organization of Bone Begins at the Nanoscale. *Science* **2018**, *360* (6388), eaao2189. https://doi.org/10.1126/science.aao2189.

(13)   Gordon, L. M.; Cohen, M. J.; MacRenaris, K. W.; Pasteris, J. D.; Seda, T.; Joester, D. Amorphous Intergranular Phases Control the Properties of Rodent Tooth Enamel. *Science* **2015**, *347* (6223), 746–750. https://doi.org/10.1126/science.1258950.

(14)   Macías-Sánchez, E.; Willinger, M. G.; Pina, C. M.; Checa, A. G. Transformation of ACC into Aragonite and the Origin of the Nanogranular Structure of Nacre. *Sci. Rep.* **2017**, *7* (1). https://doi.org/10.1038/s41598-017-12673-0.

(15)   Weaver, J. C.; Milliron, G. W.; Miserez, A.; Evans-Lutterodt, K.; Herrera, S.; Gallana, I.; Mershon, W. J.; Swanson, B.; Zavattieri, P.; DiMasi, E.; Kisailus, D. The Stomatopod Dactyl Club: A Formidable Damage-Tolerant Biological Hammer. *Science* **2012**, *336* (6086), 1275–1280. https://doi.org/10.1126/science.1218764.

(16)   Aizenberg, J.; Tkachenko, A.; Weiner, S.; Addadi, L.; Hendler, G. Calcitic Microlenses as Part of the Photoreceptor System in Brittlestars. *Nature* **2001**, *412* (6849), 819–822. https://doi.org/10.1038/35090573.

573   (17)   Nassif, N.; Martineau, F.; Syzgantseva, O.; Gobeaux, F.; Willinger, M.; Coradin, T.;
574   Cassaignon, S.; Azaïs, T.; Giraud-Guille, M. M. *In Vivo* Inspired Conditions to
575   Synthesize Biomimetic Hydroxyapatite. *Chem. Mater.* **2010**, *22* (12), 3653–3663.
576   https://doi.org/10.1021/cm903596q.
577   (18)   Nebel, H.; Epple, M. Continuous Preparation of Calcite, Aragonite and Vaterite, and of
578   Magnesium-Substituted Amorphous Calcium Carbonate (Mg-ACC). *Z. Für Anorg.*
579   *Allg. Chem.* **2008**, *634* (8), 1439–1443. https://doi.org/10.1002/zaac.200800134.
580   (19)   Ma, M.; Wang, Y.; Cao, X.; Lu, W.; Guo, Y. Temperature and Supersaturation as Key
581   Parameters Controlling the Spontaneous Precipitation of Calcium Carbonate with
582   Distinct Physicochemical Properties from Pure Aqueous Solutions. *Cryst. Growth Des.*
583   **2019**, *19* (12), 6972–6988. https://doi.org/10.1021/acs.cgd.9b00758.
584   (20)   Zeng, M.; Kim, Y.-Y.; Anduix-Canto, C.; Frontera, C.; Laundy, D.; Kapur, N.;
585   Christenson, H. K.; Meldrum, F. C. Confinement Generates Single-Crystal Aragonite
586   Rods at Room Temperature. *Proc. Natl. Acad. Sci.* **2018**, *115* (30), 7670–7675.
587   https://doi.org/10.1073/pnas.1718926115.
588   (21)   Wang, Y.; Zeng, M.; Meldrum, F. C.; Christenson, H. K. Using Confinement To Study
589   the Crystallization Pathway of Calcium Carbonate. *Cryst. Growth Des.* **2017**, *17* (12),
590   6787–6792. https://doi.org/10.1021/acs.cgd.7b01359.
591   (22)   Cantaert, B.; Beniash, E.; Meldrum, F. C. Nanoscale Confinement Controls the
592   Crystallization of Calcium Phosphate: Relevance to Bone Formation. *Chem. - Eur. J.*
593   **2013**, *19* (44), 14918–14924. https://doi.org/10.1002/chem.201302835.
594   (23)   Wang, Y.; Von Euw, S.; Laurent, G.; Crevant, C.; Bonhomme-Coury, L.; Giraud-
595   Guille, M.-M.; Babonneau, F.; Nassif, N.; Azaïs, T. Impact of Collagen Confinement
596   vs. Ionic Substitutions on the Local Disorder in Bone and Biomimetic Apatites. *Mater*
597   *Horiz* **2014**, *1* (2), 224–231. https://doi.org/10.1039/C3MH00071K.
598   (24)   Shao, C.; Jin, B.; Mu, Z.; Lu, H.; Zhao, Y.; Wu, Z.; Yan, L.; Zhang, Z.; Zhou, Y.; Pan,
599   H.; Liu, Z.; Tang, R. Repair of Tooth Enamel by a Biomimetic Mineralization Frontier
600   Ensuring Epitaxial Growth. *Sci. Adv.* **2019**, *5* (8), eaaw9569.
601   https://doi.org/10.1126/sciadv.aaw9569.
602   (25)   Olszta, M. J.; Odom, D. J.; Douglas, E. P.; Gower, L. B. A New Paradigm for
603   Biomineral Formation: Mineralization via an Amorphous Liquid-Phase Precursor.
604   *Connect. Tissue Res.* **2003**, *44* (1), 326–334.
605   https://doi.org/10.1080/03008200390181852.
606   (26)   Yao, S.; Lin, X.; Xu, Y.; Chen, Y.; Qiu, P.; Shao, C.; Jin, B.; Mu, Z.; Sommerdijk, N.
607   A. J. M.; Tang, R. Osteoporotic Bone Recovery by a Highly Bone-Inductive Calcium
608   Phosphate Polymer-Induced Liquid-Precursor. *Adv. Sci.* **2019**, *6* (19), 1900683.
609   https://doi.org/10.1002/advs.201900683.
610   (27)   Thula, T. T.; Svedlund, F.; Rodriguez, D. E.; Podschun, J.; Pendi, L.; Gower, L. B.
611   Mimicking the Nanostructure of Bone: Comparison of Polymeric Process-Directing
612   Agents. *Polymers* **2010**, *3* (1), 10–35. https://doi.org/10.3390/polym3010010.
613   (28)   Demmert, B.; Schinzel, F.; Schüßler, M.; Mondeshki, M.; Kaschta, J.; Schubert, D. W.;
614   Jacob, D. E.; Wolf, S. E. Polymer-Functionalised Nanograins of Mg-Doped
615   Amorphous Calcium Carbonate via a Flow-Chemistry Approach. *Materials* **2019**, *12*
616   (11), 1818. https://doi.org/10.3390/ma12111818.
617   (29)   Zou, Z.; Bertinetti, L.; Politi, Y.; Fratzl, P.; Habraken, W. J. E. M. Control of
618   Polymorph Selection in Amorphous Calcium Carbonate Crystallization by
619   Poly(Aspartic Acid): Two Different Mechanisms. *Small* **2017**, *13* (21), 1603100.
620   https://doi.org/10.1002/smll.201603100.

621   (30)   Ruiz-Agudo, C.; Lutz, J.; Keckeis, P.; King, M.; Marx, A.; Gebauer, D. Ubiquitin
622   Designer Proteins as a New Additive Generation toward Controlling Crystallization. *J.*
623   *Am. Chem. Soc.* **2019**, *141* (31), 12240–12245. https://doi.org/10.1021/jacs.9b06473.
624   (31)   He, G.; Dahl, T.; Veis, A.; George, A. Nucleation of Apatite Crystals in Vitro by Self-
625   Assembled Dentin Matrix Protein 1. *Nat. Mater.* **2003**, *2* (8), 552–558.
626   https://doi.org/10.1038/nmat945.
627   (32)   Gavriel, R.; Nadav-Tsubery, M.; Glick, Y.; Yarmolenko, A.; Kofman, R.; Keinan-
628   Adamsky, K.; Berman, A.; Mass, T.; Goobes, G. The Coral Protein CARP3 Acts from
629   a Disordered Mineral Surface Film to Divert Aragonite Crystallization in Favor of Mg-
630   Calcite. *Adv. Funct. Mater.* **2018**, *28* (21), 1707321.
631   https://doi.org/10.1002/adfm.201707321.
632   (33)   Elsharkawy, S.; Al-Jawad, M.; Pantano, M. F.; Tejeda-Montes, E.; Mehta, K.; Jamal,
633   H.; Agarwal, S.; Shuturminska, K.; Rice, A.; Tarakina, N. V.; Wilson, R. M.; Bushby,
634   A. J.; Alonso, M.; Rodriguez-Cabello, J. C.; Barbieri, E.; del Río Hernández, A.;
635   Stevens, M. M.; Pugno, N. M.; Anderson, P.; Mata, A. Protein Disorder–Order
636   Interplay to Guide the Growth of Hierarchical Mineralized Structures. *Nat. Commun.*
637   **2018**, *9* (1), 2145. https://doi.org/10.1038/s41467-018-04319-0.
638   (34)   Green, D. C.; Shida, Y.; Honma, N.; Holden, M. A.; Kim, Y.-Y.; Kulak, A. N.;
639   Ogasawara, W.; Meldrum, F. C. Skin-Deep Surface Patterning of Calcite. *Chem.*
640   *Mater.* **2019**, *31* (21), 8725–8733. https://doi.org/10.1021/acs.chemmater.9b02421.
641   (35)   Evans, D.; Webb, P. B.; Penkman, K.; Kröger, R.; Allison, N. The Characteristics and
642   Biological Relevance of Inorganic Amorphous Calcium Carbonate (ACC) Precipitated
643   from Seawater. *Cryst. Growth Des.* **2019**, *19* (8), 4300–4313.
644   https://doi.org/10.1021/acs.cgd.9b00003.
645   (36)   Štajner, L.; Kontrec, J.; Njegić Džakula, B.; Maltar-Strmečki, N.; Plodinec, M.; Lyons,
646   D. M.; Kralj, D. The Effect of Different Amino Acids on Spontaneous Precipitation of
647   Calcium Carbonate Polymorphs. *J. Cryst. Growth* **2018**, *486*, 71–81.
648   https://doi.org/10.1016/j.jcrysgro.2018.01.023.
649   (37)   Tobler, D. J.; Blanco, J. D. R.; Dideriksen, K.; Sand, K. K.; Bovet, N.; Benning, L. G.;
650   Stipp, S. L. S. The Effect of Aspartic Acid and Glycine on Amorphous Calcium
651   Carbonate (ACC) Structure, Stability and Crystallization. *Procedia Earth Planet. Sci.*
652   **2014**, *10*, 143–148. https://doi.org/10.1016/j.proeps.2014.08.047.
653   (38)   Pouget, E. M.; Bomans, P. H. H.; Goos, J. A. C. M.; Frederik, P. M.; de With, G.;
654   Sommerdijk, N. A. J. M. The Initial Stages of Template-Controlled CaCO3 Formation
655   Revealed by Cryo-TEM. *Science* **2009**, *323* (5920), 1455–1458.
656   https://doi.org/10.1126/science.1169434.
657   (39)   Gebauer, D.; Völkel, A.; Cölfen, H. Stable Prenucleation Calcium Carbonate Clusters.
658   *Science* **2008**, *322* (5909), 1819–1822. https://doi.org/10.1126/science.1164271.
659   (40)   Dey, A.; Bomans, P. H. H.; Müller, F. A.; Will, J.; Frederik, P. M.; de With, G.;
660   Sommerdijk, N. A. J. M. The Role of Prenucleation Clusters in Surface-Induced
661   Calcium Phosphate Crystallization. *Nat. Mater.* **2010**, *9* (12), 1010–1014.
662   https://doi.org/10.1038/nmat2900.
663   (41)   Gebauer, D.; Kellermeier, M.; Gale, J. D.; Bergström, L.; Cölfen, H. Pre-Nucleation
664   Clusters as Solute Precursors in Crystallisation. *Chem Soc Rev* **2014**, *43* (7), 2348–
665   2371. https://doi.org/10.1039/C3CS60451A.
666   (42)   Gebauer, D.; Wolf, S. E. Designing Solid Materials from Their Solute State: A Shift in
667   Paradigms toward a Holistic Approach in Functional Materials Chemistry. *J. Am.*
668   *Chem. Soc.* **2019**, *141* (11), 4490–4504. https://doi.org/10.1021/jacs.8b13231.
669   (43)   Wang, Y.; Azaïs, T.; Robin, M.; Vallée, A.; Catania, C.; Legriel, P.; Pehau-Arnaudet,
670   G.; Babonneau, F.; Giraud-Guille, M.-M.; Nassif, N. The Predominant Role of

Collagen in the Nucleation, Growth, Structure and Orientation of Bone Apatite. *Nat. Mater.* **2012**, *11* (8), 724–733. https://doi.org/10.1038/nmat3362.

(44) Thrivikraman, G.; Athirasala, A.; Gordon, R.; Zhang, L.; Bergan, R.; Keene, D. R.; Jones, J. M.; Xie, H.; Chen, Z.; Tao, J.; Wingender, B.; Gower, L.; Ferracane, J. L.; Bertassoni, L. E. Rapid Fabrication of Vascularized and Innervated Cell-Laden Bone Models with Biomimetic Intrafibrillar Collagen Mineralization. *Nat. Commun.* **2019**, *10* (1), 3520. https://doi.org/10.1038/s41467-019-11455-8.

(45) Wingender, B.; Bradley, P.; Saxena, N.; Ruberti, J. W.; Gower, L. Biomimetic Organization of Collagen Matrices to Template Bone-like Microstructures. *Matrix Biol.* **2016**, *52–54*, 384–396. https://doi.org/10.1016/j.matbio.2016.02.004.

(46) Volkmer, D.; Harms, M.; Gower, L.; Ziegler, A. Morphosynthesis of Nacre-Type Laminated CaCO3 Thin Films and Coatings. *Angew. Chem. Int. Ed.* **2005**, *44* (4), 639–644. https://doi.org/10.1002/anie.200461386.

(47) Mao, L.-B.; Gao, H.-L.; Yao, H.-B.; Liu, L.; Colfen, H.; Liu, G.; Chen, S.-M.; Li, S.-K.; Yan, Y.-X.; Liu, Y.-Y.; Yu, S.-H. Synthetic Nacre by Predesigned Matrix-Directed Mineralization. *Science* **2016**, *354* (6308), 107–110. https://doi.org/10.1126/science.aaf8991.

(48) Wingender, B.; Ni, Y.; Zhang, Y.; Taylor, C.; Gower, L. Hierarchical Characterization and Nanomechanical Assessment of Biomimetic Scaffolds Mimicking Lamellar Bone via Atomic Force Microscopy Cantilever-Based Nanoindentation. *Materials* **2018**, *11* (7), 1257. https://doi.org/10.3390/ma11071257.

(49) Von Euw, S.; Zhang, Q.; Manichev, V.; Murali, N.; Gross, J.; Feldman, L. C.; Gustafsson, T.; Flach, C.; Mendelsohn, R.; Falkowski, P. G. Biological Control of Aragonite Formation in Stony Corals. *Science* **2017**, *356* (6341), 933–938. https://doi.org/10.1126/science.aam6371.

(50) Beniash, E.; Metzler, R. A.; Lam, R. S. K.; Gilbert, P. U. P. A. Transient Amorphous Calcium Phosphate in Forming Enamel. *J. Struct. Biol.* **2009**, *166* (2), 133–143. https://doi.org/10.1016/j.jsb.2009.02.001.

(51) Mahamid, J.; Sharir, A.; Addadi, L.; Weiner, S. Amorphous Calcium Phosphate Is a Major Component of the Forming Fin Bones of Zebrafish: Indications for an Amorphous Precursor Phase. *Proc. Natl. Acad. Sci.* **2008**, *105* (35), 12748–12753. https://doi.org/10.1073/pnas.0803354105.

(52) Politi, Y.; Metzler, R. A.; Abrecht, M.; Gilbert, B.; Wilt, F. H.; Sagi, I.; Addadi, L.; Weiner, S.; Gilbert, P. U. P. A. Transformation Mechanism of Amorphous Calcium Carbonate into Calcite in the Sea Urchin Larval Spicule. *Proc. Natl. Acad. Sci.* **2008**, *105* (45), 17362–17366. https://doi.org/10.1073/pnas.0806604105.

(53) DeVol, R. T.; Sun, C.-Y.; Marcus, M. A.; Coppersmith, S. N.; Myneni, S. C. B.; Gilbert, P. U. P. A. Nanoscale Transforming Mineral Phases in Fresh Nacre. *J. Am. Chem. Soc.* **2015**, *137* (41), 13325–13333. https://doi.org/10.1021/jacs.5b07931.

(54) Beniash, E.; Aizenberg, J.; Addadi, L.; Weiner, S. Amorphous Calcium Carbonate Transforms into Calcite during Sea Urchin Larval Spicule Growth. *Proc. R. Soc. Lond. B Biol. Sci.* **1997**, *264* (1380), 461–465. https://doi.org/10.1098/rspb.1997.0066.

(55) Weiss, I. M.; Tuross, N.; Addadi, L.; Weiner, S. Mollusc Larval Shell Formation: Amorphous Calcium Carbonate Is a Precursor Phase for Aragonite. *J. Exp. Zool.* **2002**, *293* (5), 478–491. https://doi.org/10.1002/jez.90004.

(56) Griesshaber, E.; Kelm, K.; Sehrbrock, A.; Mader, W.; Mutterlose, J.; Brand, U.; Schmahl, W. W. Amorphous Calcium Carbonate in the Shell Material of the Brachiopod Megerlia Truncata. *Eur. J. Mineral.* **2009**, *21* (4), 715–723. https://doi.org/10.1127/0935-1221/2009/0021-1950.

(57) Mass, T.; Giuffre, A. J.; Sun, C.-Y.; Stifler, C. A.; Frazier, M. J.; Neder, M.; Tamura, N.; Stan, C. V.; Marcus, M. A.; Gilbert, P. U. P. A. Amorphous Calcium Carbonate Particles Form Coral Skeletons. *Proc. Natl. Acad. Sci.* **2017**, *114* (37), E7670–E7678. https://doi.org/10.1073/pnas.1707890114.

(58) Politi, Y. Sea Urchin Spine Calcite Forms via a Transient Amorphous Calcium Carbonate Phase. *Science* **2004**, *306* (5699), 1161–1164. https://doi.org/10.1126/science.1102289.

(59) Polishchuk, I.; Bracha, A. A.; Bloch, L.; Levy, D.; Kozachkevich, S.; Etinger-Geller, Y.; Kauffmann, Y.; Burghammer, M.; Giacobbe, C.; Villanova, J.; Hendler, G.; Sun, C.-Y.; Giuffre, A. J.; Marcus, M. A.; Kundanati, L.; Zaslansky, P.; Pugno, N. M.; Gilbert, P. U. P. A.; Katsman, A.; Pokroy, B. Coherently Aligned Nanoparticles within a Biogenic Single Crystal: A Biological Prestressing Strategy. *Science* **2017**, *358* (6368), 1294–1298. https://doi.org/10.1126/science.aaj2156.

(60) Gal, A.; Habraken, W.; Gur, D.; Fratzl, P.; Weiner, S.; Addadi, L. Calcite Crystal Growth by a Solid-State Transformation of Stabilized Amorphous Calcium Carbonate Nanospheres in a Hydrogel. *Angew. Chem. Int. Ed.* **2013**, *52* (18), 4867–4870. https://doi.org/10.1002/anie.201210329.

(61) Sun, R.; Willhammar, T.; Svensson Grape, E.; Strømme, M.; Cheung, O. Mesoscale Transformation of Amorphous Calcium Carbonate to Porous Vaterite Microparticles with Morphology Control. *Cryst. Growth Des.* **2019**, *19* (9), 5075–5087. https://doi.org/10.1021/acs.cgd.9b00438.

(62) Schweikle, M.; Bjørnøy, S. H.; van Helvoort, A. T. J.; Haugen, H. J.; Sikorski, P.; Tiainen, H. Stabilisation of Amorphous Calcium Phosphate in Polyethylene Glycol Hydrogels. *Acta Biomater.* **2019**, *90*, 132–145. https://doi.org/10.1016/j.actbio.2019.03.044.

(63) Cantaert, B.; Kuo, D.; Matsumura, S.; Nishimura, T.; Sakamoto, T.; Kato, T. Use of Amorphous Calcium Carbonate for the Design of New Materials. *ChemPlusChem* **2017**, *82* (1), 107–120. https://doi.org/10.1002/cplu.201600457.

(64) Yu, Y.; He, Y.; Mu, Z.; Zhao, Y.; Kong, K.; Liu, Z.; Tang, R. Biomimetic Mineralized Organic–Inorganic Hybrid Macrofiber with Spider Silk-Like Supertoughness. *Adv. Funct. Mater.* **2020**, *30* (6), 1908556. https://doi.org/10.1002/adfm.201908556.

(65) Weiner, S.; Levi-Kalisman, Y.; Raz, S.; Addadi, L. Biologically Formed Amorphous Calcium Carbonate. *Connect. Tissue Res.* **2003**, *44 Suppl 1*, 214–218.

(66) Shapiro, O. H.; Kartvelishvily, E.; Kramarsky-Winter, E.; Vardi, A. Magnesium-Rich Nanometric Layer in the Skeleton of Pocillopora Damicornis With Possible Involvement in Fibrous Aragonite Deposition. *Front. Mar. Sci.* **2018**, *5*, 246. https://doi.org/10.3389/fmars.2018.00246.

(67) Nebel, H.; Neumann, M.; Mayer, C.; Epple, M. On the Structure of Amorphous Calcium Carbonate - A Detailed Study by Solid-State NMR Spectroscopy. *Inorg. Chem.* **2008**, *47* (17), 7874–7879. https://doi.org/10.1021/ic8007409.

(68) Gebauer, D.; Gunawidjaja, P. N.; Ko, J. Y. P.; Bacsik, Z.; Aziz, B.; Liu, L.; Hu, Y.; Bergström, L.; Tai, C.-W.; Sham, T.-K.; Edén, M.; Hedin, N. Proto-Calcite and Proto-Vaterite in Amorphous Calcium Carbonates. *Angew. Chem. Int. Ed.* **2010**, *49* (47), 8889–8891. https://doi.org/10.1002/anie.201003220.

(69) Michel, F. M.; MacDonald, J.; Feng, J.; Phillips, B. L.; Ehm, L.; Tarabrella, C.; Parise, J. B.; Reeder, R. J. Structural Characteristics of Synthetic Amorphous Calcium Carbonate. *Chem. Mater.* **2008**, *20* (14), 4720–4728. https://doi.org/10.1021/cm800324v.

(70) Yang, S.-Y.; Chang, H.-H.; Lin, C.-J.; Huang, S.-J.; Chan, J. C. C. Is Mg-Stabilized Amorphous Calcium Carbonate a Homogeneous Mixture of Amorphous Magnesium

Carbonate and Amorphous Calcium Carbonate? *Chem. Commun.* **2016**, *52* (77), 11527–11530. https://doi.org/10.1039/C6CC04522G.

(71) Leukel, S.; Mondeshki, M.; Tremel, W. Hydrogen Bonding in Amorphous Alkaline Earth Carbonates. *Inorg. Chem.* **2018**, *57* (17), 11289–11298. https://doi.org/10.1021/acs.inorgchem.8b02170.

(72) Von Euw, S.; Wang, Y.; Laurent, G.; Drouet, C.; Babonneau, F.; Nassif, N.; Azaïs, T. Bone Mineral: New Insights into Its Chemical Composition. *Sci. Rep.* **2019**, *9* (1). https://doi.org/10.1038/s41598-019-44620-6.

(73) Sideris, P. J.; Nielsen, U. G.; Gan, Z.; Grey, C. P. Mg/Al Ordering in Layered Double Hydroxides Revealed by Multinuclear NMR Spectroscopy. *Science* **2008**, *321* (5885), 113–117. https://doi.org/10.1126/science.1157581.

(74) Gaffey, S. J. H_2O and OH in Echinoid Calcite; a Spectroscopic Study. *Am. Mineral.* **1995**, *80* (9–10), 947–959. https://doi.org/10.2138/am-1995-9-1011.

(75) Pourpoint, F.; Gervais, C.; Bonhomme-Coury, L.; Azaïs, T.; Coelho, C.; Mauri, F.; Alonso, B.; Babonneau, F.; Bonhomme, C. Calcium Phosphates and Hydroxyapatite: Solid-State NMR Experiments and First-Principles Calculations. *Appl. Magn. Reson.* **2007**, *32* (4), 435–457. https://doi.org/10.1007/s00723-007-0040-1.

(76) Bird, M. I.; Chivas, A. R.; Radnell, C. J.; Burton, H. R. Sedimentological and Stable-Isotope Evolution of Lakes in the Vestfold Hills, Antarctica. *Palaeogeogr. Palaeoclimatol. Palaeoecol.* **1991**, *84* (1–4), 109–130. https://doi.org/10.1016/0031-0182(91)90039-T.

(77) Onac, B. P. Mineralogical Studies and Uranium-Series Dating of Speleothems from Scarisoara Glacier Cave (Bihor Mountains, Romania). *Theor. Appl. Karstology* **2001**, *13–14*, 33–38.

(78) Carlström, D. A CRYSTALLOGRAPHIC STUDY OF VERTEBRATE OTOLITHS. *Biol. Bull.* **1963**, *125* (3), 441–463. https://doi.org/10.2307/1539358.

(79) Señorale-Pose, M.; Chalar, C.; Dauphin, Y.; Massard, P.; Pradel, P.; Marín, M. Monohydrocalcite in Calcareous Corpuscles of Mesocestoides Corti. *Exp. Parasitol.* **2008**, *118* (1), 54–58. https://doi.org/10.1016/j.exppara.2007.06.011.

(80) Catherine, H.; Skinner, W.; Osbaldiston, G. W.; Wilner, A. N. Monohydrocalcite in a Guinea Pig Bladder Stone, a Novel Occurrence. *Am. Mineral.* **1977**, *62* (3–4), 273–277.

(81) Rodriguez-Blanco, J. D.; Shaw, S.; Bots, P.; Roncal-Herrero, T.; Benning, L. G. The Role of Mg in the Crystallization of Monohydrocalcite. *Geochim. Cosmochim. Acta* **2014**, *127*, 204–220. https://doi.org/10.1016/j.gca.2013.11.034.

(82) Konrad, F.; Purgstaller, B.; Gallien, F.; Mavromatis, V.; Gane, P.; Dietzel, M. Influence of Aqueous Mg Concentration on the Transformation of Amorphous Calcium Carbonate. *J. Cryst. Growth* **2018**, *498*, 381–390. https://doi.org/10.1016/j.jcrysgro.2018.07.018.

(83) Loste, E.; Wilson, R. M.; Seshadri, R.; Meldrum, F. C. The Role of Magnesium in Stabilising Amorphous Calcium Carbonate and Controlling Calcite Morphologies. *J. Cryst. Growth* **2003**, *254* (1–2), 206–218. https://doi.org/10.1016/S0022-0248(03)01153-9.

(84) Huang, Y.-C.; Gindele, M. B.; Knaus, J.; Rao, A.; Gebauer, D. On Mechanisms of Mesocrystal Formation: Magnesium Ions and Water Environments Regulate the Crystallization of Amorphous Minerals. *CrystEngComm* **2018**, *20* (31), 4395–4405. https://doi.org/10.1039/C8CE00241J.

(85) Nishiyama, R.; Munemoto, T.; Fukushi, K. Formation Condition of Monohydrocalcite from CaCl2–MgCl2–Na2CO3 Solutions. *Geochim. Cosmochim. Acta* **2013**, *100*, 217–231. https://doi.org/10.1016/j.gca.2012.09.002.

(86) Wang, Y.-Y.; Yao, Q.-Z.; Zhou, G.-T.; Fu, S.-Q. Transformation of Amorphous Calcium Carbonate into Monohydrocalcite in Aqueous Solution: A Biomimetic Mineralization Study. *Eur. J. Mineral.* **2015**, *27* (6), 717–729. https://doi.org/10.1127/ejm/2015/0027-2486.

(87) Kimura, T.; Koga, N. Monohydrocalcite in Comparison with Hydrated Amorphous Calcium Carbonate: Precipitation Condition and Thermal Behavior. *Cryst. Growth Des.* **2011**, *11* (9), 3877–3884. https://doi.org/10.1021/cg200412h.

(88) Giuffre, A. J.; Gagnon, A. C.; De Yoreo, J. J.; Dove, P. M. Isotopic Tracer Evidence for the Amorphous Calcium Carbonate to Calcite Transformation by Dissolution–Reprecipitation. *Geochim. Cosmochim. Acta* **2015**, *165*, 407–417. https://doi.org/10.1016/j.gca.2015.06.002.

(89) Liu, Z.; Zhang, Z.; Wang, Z.; Jin, B.; Li, D.; Tao, J.; Tang, R.; De Yoreo, J. J. Shape-Preserving Amorphous-to-Crystalline Transformation of CaCO₃ Revealed by in Situ TEM. *Proc. Natl. Acad. Sci.* **2020**, *117* (7), 3397–3404. https://doi.org/10.1073/pnas.1914813117.

(90) Bots, P.; Benning, L. G.; Rodriguez-Blanco, J.-D.; Roncal-Herrero, T.; Shaw, S. Mechanistic Insights into the Crystallization of Amorphous Calcium Carbonate (ACC). *Cryst. Growth Des.* **2012**, *12* (7), 3806–3814. https://doi.org/10.1021/cg300676b.

(91) Rodriguez-Blanco, J. D.; Shaw, S.; Benning, L. G. The Kinetics and Mechanisms of Amorphous Calcium Carbonate (ACC) Crystallization to Calcite, via Vaterite. *Nanoscale* **2011**, *3* (1), 265–271. https://doi.org/10.1039/C0NR00589D.

(92) Rodriguez-Blanco, J. D.; Shaw, S.; Bots, P.; Roncal-Herrero, T.; Benning, L. G. The Role of PH and Mg on the Stability and Crystallization of Amorphous Calcium Carbonate. *J. Alloys Compd.* **2012**, *536*, S477–S479. https://doi.org/10.1016/j.jallcom.2011.11.057.

(93) Albéric, M.; Bertinetti, L.; Zou, Z.; Fratzl, P.; Habraken, W.; Politi, Y. The Crystallization of Amorphous Calcium Carbonate Is Kinetically Governed by Ion Impurities and Water. *Adv. Sci.* **2018**, *5* (5), 1701000. https://doi.org/10.1002/advs.201701000.

(94) Du, H.; Steinacher, M.; Borca, C.; Huthwelker, T.; Murello, A.; Stellacci, F.; Amstad, E. Amorphous CaCO₃: Influence of the Formation Time on Its Degree of Hydration and Stability. *J. Am. Chem. Soc.* **2018**, *140* (43), 14289–14299. https://doi.org/10.1021/jacs.8b08298.

(95) Wang, Y.; Von Euw, S.; Fernandes, F. M.; Cassaignon, S.; Selmane, M.; Laurent, G.; Pehau-Arnaudet, G.; Coelho, C.; Bonhomme-Coury, L.; Giraud-Guille, M.-M.; Babonneau, F.; Azaïs, T.; Nassif, N. Water-Mediated Structuring of Bone Apatite. *Nat. Mater.* **2013**, *12* (12), 1144–1153. https://doi.org/10.1038/nmat3787.

(96) Neumann, M.; Epple, M. Monohydrocalcite and Its Relationship to Hydrated Amorphous Calcium Carbonate in Biominerals. *Eur. J. Inorg. Chem.* **2007**, *2007* (14), 1953–1957. https://doi.org/10.1002/ejic.200601033.

(97) Dauphin, Y. Nanostructures of the nacreous layers in Recent cephalopod shells. *Paläontol. Z.* **2001**, *75* (1), 113–122. https://doi.org/10.1007/BF03022601.

(98) Gilbert, P. U. P. A.; Porter, S. M.; Sun, C.-Y.; Xiao, S.; Gibson, B. M.; Shenkar, N.; Knoll, A. H. Biomineralization by Particle Attachment in Early Animals. *Proc. Natl. Acad. Sci.* **2019**, *116* (36), 17659–17665. https://doi.org/10.1073/pnas.1902273116.

(99) Gal, A.; Kahil, K.; Vidavsky, N.; DeVol, R. T.; Gilbert, P. U. P. A.; Fratzl, P.; Weiner, S.; Addadi, L. Particle Accretion Mechanism Underlies Biological Crystal Growth from an Amorphous Precursor Phase. *Adv. Funct. Mater.* **2014**, *24* (34), 5420–5426. https://doi.org/10.1002/adfm.201400676.

868 (100) Gal, A.; Weiner, S.; Addadi, L. A Perspective on Underlying Crystal Growth
869 Mechanisms in Biomineralization: Solution Mediated Growth versus Nanosphere
870 Particle Accretion. *CrystEngComm* **2015**, *17* (13), 2606–2615.
871 https://doi.org/10.1039/C4CE01474J.
872 (101) De Yoreo, J. J.; Gilbert, P. U. P. A.; Sommerdijk, N. A. J. M.; Penn, R. L.; Whitelam,
873 S.; Joester, D.; Zhang, H.; Rimer, J. D.; Navrotsky, A.; Banfield, J. F.; Wallace, A. F.;
874 Michel, F. M.; Meldrum, F. C.; Colfen, H.; Dove, P. M. Crystallization by Particle
875 Attachment in Synthetic, Biogenic, and Geologic Environments. *Science* **2015**, *349*
876 (6247), aaa6760–aaa6760. https://doi.org/10.1126/science.aaa6760.
877 (102) Walker, J. M.; Marzec, B.; Nudelman, F. Solid-State Transformation of Amorphous
878 Calcium Carbonate to Aragonite Captured by CryoTEM. *Angew. Chem.* **2017**, *129*
879 (39), 11902–11905. https://doi.org/10.1002/ange.201703158.
880 (103) Lin, C.-J.; Yang, S.-Y.; Huang, S.-J.; Chan, J. C. C. Structural Characterization of Mg-
881 Stabilized Amorphous Calcium Carbonate by Mg-25 Solid-State NMR Spectroscopy.
882 *J. Phys. Chem. C* **2015**, *119* (13), 7225–7233. https://doi.org/10.1021/jp512971a.
883 (104) Dorvee, J. R.; Veis, A. Water in the Formation of Biogenic Minerals: Peeling Away the
884 Hydration Layers. *J. Struct. Biol.* **2013**, *183* (2), 278–303.
885 https://doi.org/10.1016/j.jsb.2013.06.007.
886 (105) Sen, S.; Kaseman, D. C.; Colas, B.; Jacob, D. E.; Clark, S. M. Hydrogen Bonding
887 Induced Distortion of CO_3 Units and Kinetic Stabilization of Amorphous Calcium
888 Carbonate: Results from 2D ^{13}C NMR Spectroscopy. *Phys. Chem. Chem. Phys.* **2016**,
889 *18* (30), 20330–20337. https://doi.org/10.1039/C6CP02729F.
890 (106) Rodriguez-Navarro, C.; Burgos Cara, A.; Elert, K.; Putnis, C. V.; Ruiz-Agudo, E.
891 Direct Nanoscale Imaging Reveals the Growth of Calcite Crystals via Amorphous
892 Nanoparticles. *Cryst. Growth Des.* **2016**, *16* (4), 1850–1860.
893 https://doi.org/10.1021/acs.cgd.5b01180.
894 (107) Kababya, S.; Gal, A.; Kahil, K.; Weiner, S.; Addadi, L.; Schmidt, A. Phosphate–Water
895 Interplay Tunes Amorphous Calcium Carbonate Metastability: Spontaneous Phase
896 Separation and Crystallization vs Stabilization Viewed by Solid State NMR. *J. Am.*
897 *Chem. Soc.* **2015**, *137* (2), 990–998. https://doi.org/10.1021/ja511869g.
898 (108) Drake, J.; Mass, T.; Stołarski, J.; Von Euw, S.; van de Schootbrugge, B.; Falkowski, P.
899 G. How Corals Made Rocks through the Ages. *Glob. Change Biol.* **2019**, gcb.14912.
900 https://doi.org/10.1111/gcb.14912.
901 (109) Sun, C.-Y.; Marcus, M. A.; Frazier, M. J.; Giuffre, A. J.; Mass, T.; Gilbert, P. U. P. A.
902 Spherulitic Growth of Coral Skeletons and Synthetic Aragonite: Nature's Three-
903 Dimensional Printing. *ACS Nano* **2017**, *11* (7), 6612–6622.
904 https://doi.org/10.1021/acsnano.7b00127.
905

906 **Figure 1.**

907
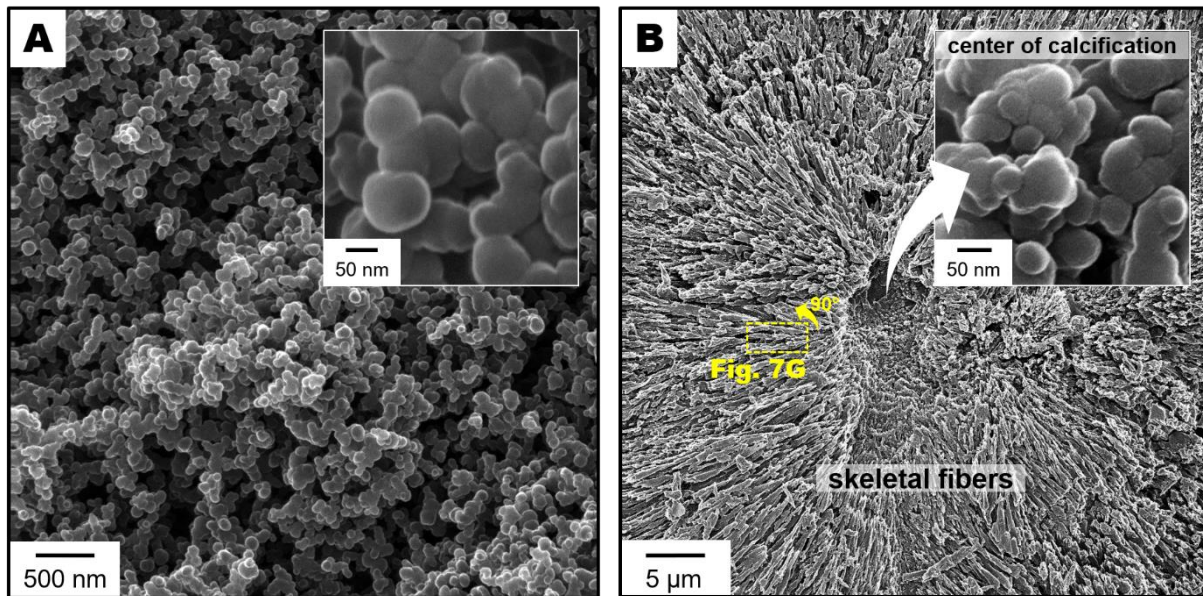
908 **Figure 1. Morphological features of synthetic and biogenic amorphous nanoparticles.**

909 Representative scanning helium ion microscopy (SHIM) micrographs of the synthetic,

910 Amorphous Calcium Magnesium Carbonate (ACMC) sample (**A**). For the purpose of

911 comparison with biogenic deposits of amorphous $CaCO_3$, also shown are representative

912 SHIM micrographs obtained from the broken, unpolished, etched-surface of a coral skeletal

913 branch that was transversely sectioned (**B**). Shown here is a trabecula composed of skeletal

914 fibers in the form of acicular aragonite crystals, that radiate from a center of calcification

915 (COC) composed of magnesium-rich, amorphous calcium carbonate nanoparticles [108].

916

917   **Figure 2.**
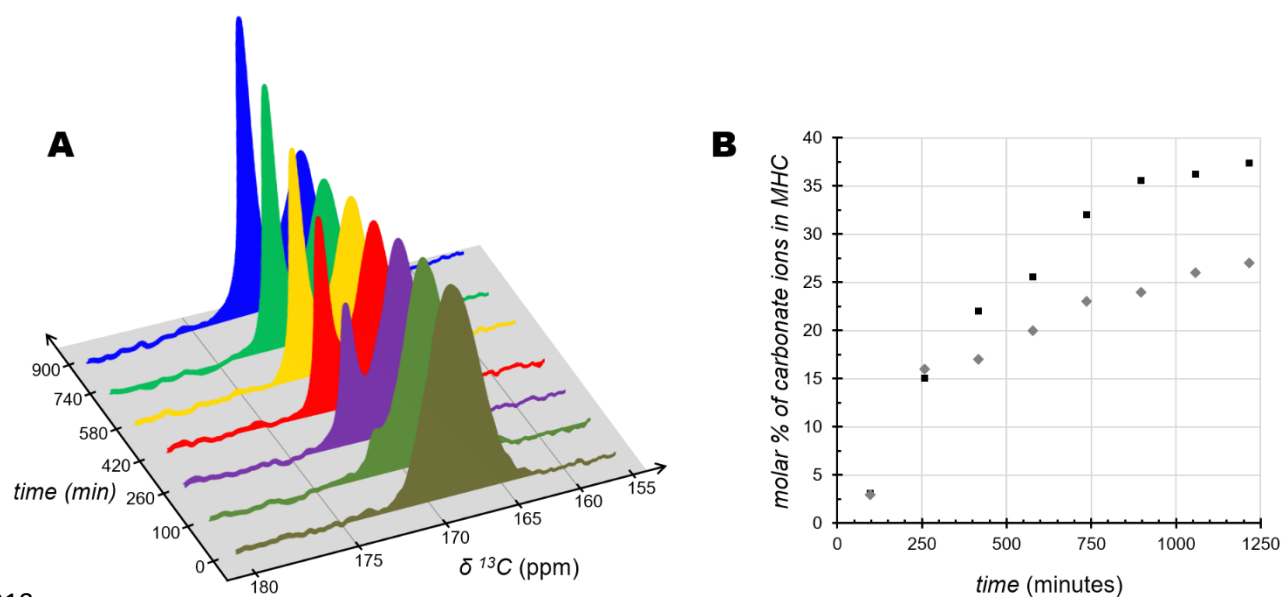
918

919   **Figure 2. Kinetics of crystallization of the synthetic amorphous nanoparticles. (A)** Non-

920   normalized 1D ^{13}C single-pulse (SP) MAS ssNMR spectra (recycling delay, RD = 600 s;

921   number of scans, NS = 8; MAS frequency, ν_{MAS} = 8 kHz) of the synthetic, Amorphous

922   Calcium Magnesium Carbonate (ACMC) sample soaked in deionized water as crystallization

923   progresses. **(B)** Conversion rate of the starting amorphous environments into

924   monohydrocalcite as a function of time for ACMC soaked in deionized water (**black squares**)

925   or heavy water (**grey squares**). This conversion rate is here expressed in terms of the molar

926   percentage of carbonate ions present in monohydrocalcite (MHC) environments.

927
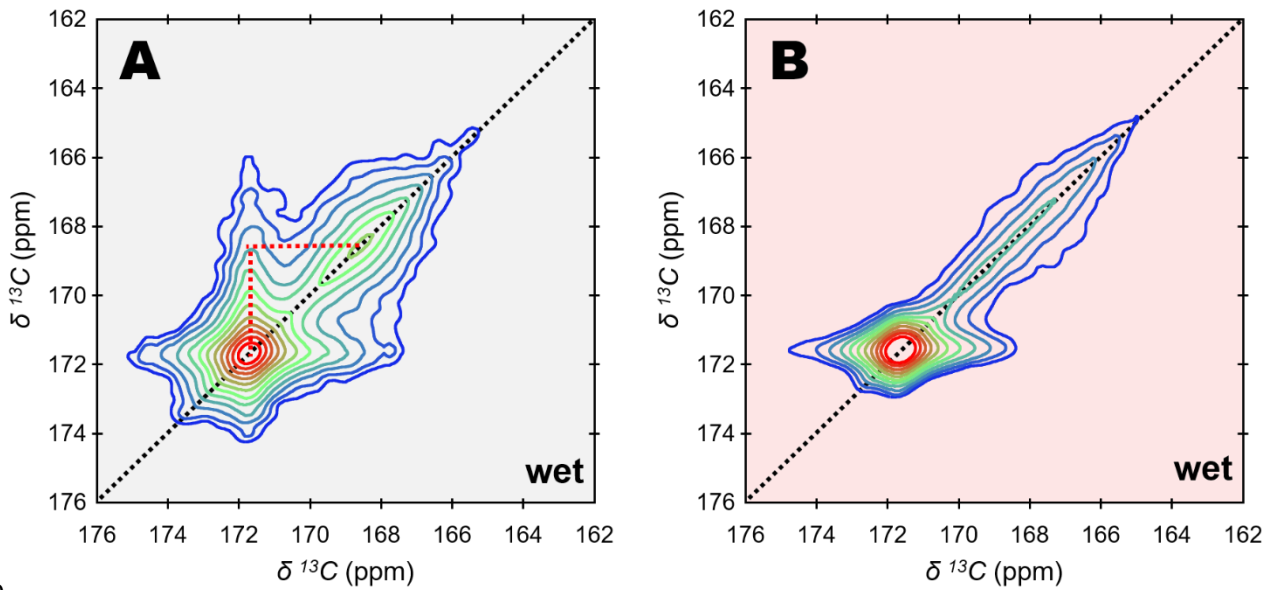
Figure 3.

929

930   **Figure 3. Spatial proximities among the carbon-bearing ions.** Contour plots of two-

931   dimensional (2D) ^{13}C-^{13}C Dipolar Assisted Rotational Resonance (DARR) MAS ssNMR

932   spectra (contact time, t_{CP} = 4 ms; mixing time, τ_{mix} = 500 ms; 8 scans in each 384 t1

933   increments; relaxation delay, RD = 1 s; MAS frequency, ν_{MAS} = 8 kHz) of the synthetic,

934   Amorphous Calcium Magnesium Carbonate (ACMC) sample soaked in deionized water, and

935   partially converted into monohydrocalcite (conversion rate, 30%) (**A**); and of a physical

936   mixture of two powders soaking in deionized water: the synthetic monohydrocalcite (MHC)

937   sample and ACMC before crystallization (**B**). The signal intensity increases from blue to red.

938 **Figure 4.**
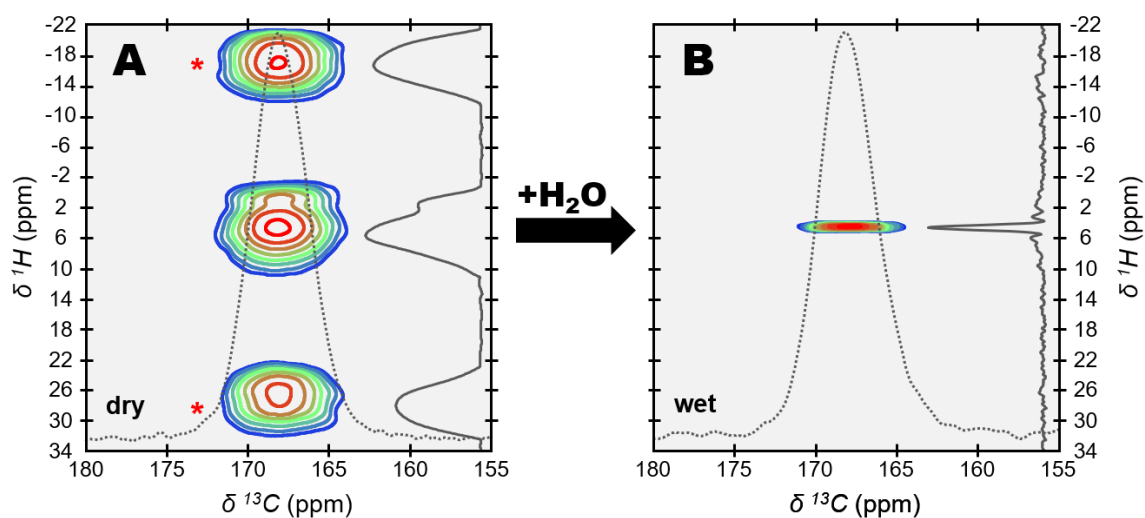
939

940 **Figure 4. Spatial proximities among carbon-bearing ions and hydrogen-bearing**

941 **ions/molecules in the amorphous nanoparticles.** Contour plots of two-dimensional (2D)

942 $\{^1H\}^{13}C$ Heteronuclear Correlation (HetCor) MAS ssNMR spectra [contact time, t_{CP} = 4 ms;

943 64 (dry conditions) or 16 (wet conditions) scans in each 120 t1 increments; relaxation delay,

944 RD = 2 s; MAS frequency, ν_{MAS} = 8 kHz] of the synthetic, Amorphous Calcium Magnesium

945 Carbonate (ACMC) sample in dry conditions (**A**) and soaked in deionized water for 50

946 minutes (**B**). The signal intensity increases from blue to red. Also shown are the normalized,

947 projections of the vertical, indirect ^1H dimensions (solid lines) and of the horizontal, direct

948 ^{13}C dimensions (dotted lines) of these two 2D $\{^1H\}^{13}C$ HetCor MAS ssNMR spectra. The red

949 asterisks (*) denote the intense spinning sidebands only seen in dry conditions.

Figure 5.

951
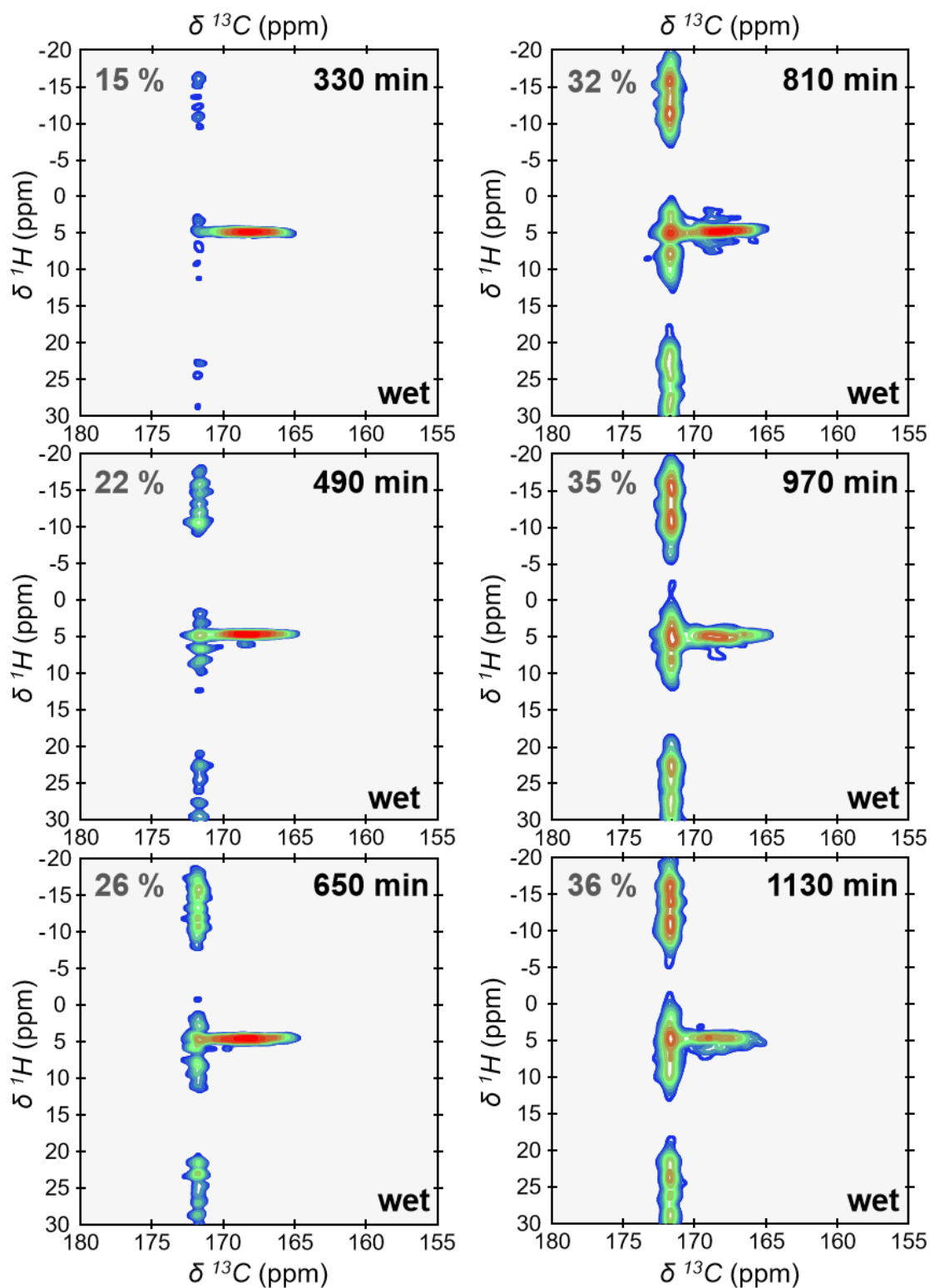
Figure 5. Evolution of the hydrogen chemical environments during crystallization.

Contour plots of 2D {¹H}¹³C Heteronuclear Correlation (HetCor) MAS ssNMR spectra

954   (contact time, t_{CP} = 4 ms; 16 scans in each 120 t1 increments; relaxation delay, RD = 2 s;

955   MAS frequency, ν_{MAS} = 8 kHz) of the synthetic, Amorphous Calcium Magnesium Carbonate

956   (ACMC) sample soaked in deionized water while crystallization progresses. The signal

957   intensity increases from blue to red. The percentages displayed in the upper left corner are the

958   conversion rate of ACMC into monohydrocalcite, whereas the values shown in the upper right

959   corner are the periods of time during which the sample has been soaking in water following

960   the initial wetting step.
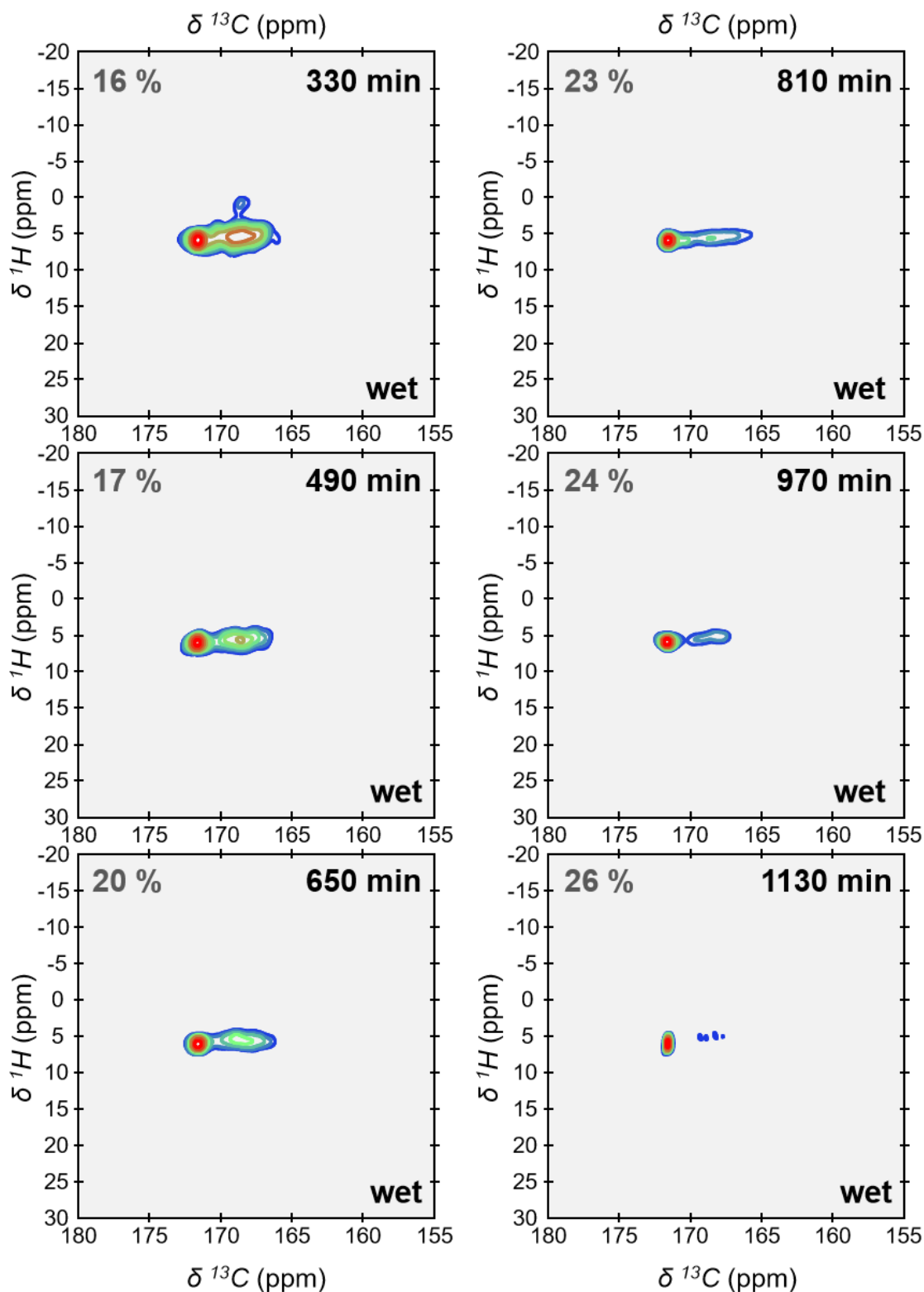
Figure 6.

Figure 6. Deuterium-hydrogen chemical exchanges during crystallization. Contour plots

of 2D {^{1}H}^{13}C Heteronuclear Correlation (HetCor) MAS ssNMR spectra (contact time, t_{CP} =

965   4 ms; 16 scans in each 120 t1 increments; relaxation delay, RD = 2 s; MAS frequency, ν_{MAS} =

966   8 kHz) of the synthetic, Amorphous Calcium Magnesium Carbonate (ACMC) sample soaked

967   in heavy water (D_2O - 99.99 atom% D) while crystallization progresses. The signal intensity

968   increases from blue to red. The percentages displayed in the upper left corner are the

969   conversion rate of ACMC into monohydrocalcite, whereas the values shown in the upper right

970   corner are the periods of time during which the sample has been soaking in heavy water

971   following the initial wetting step.
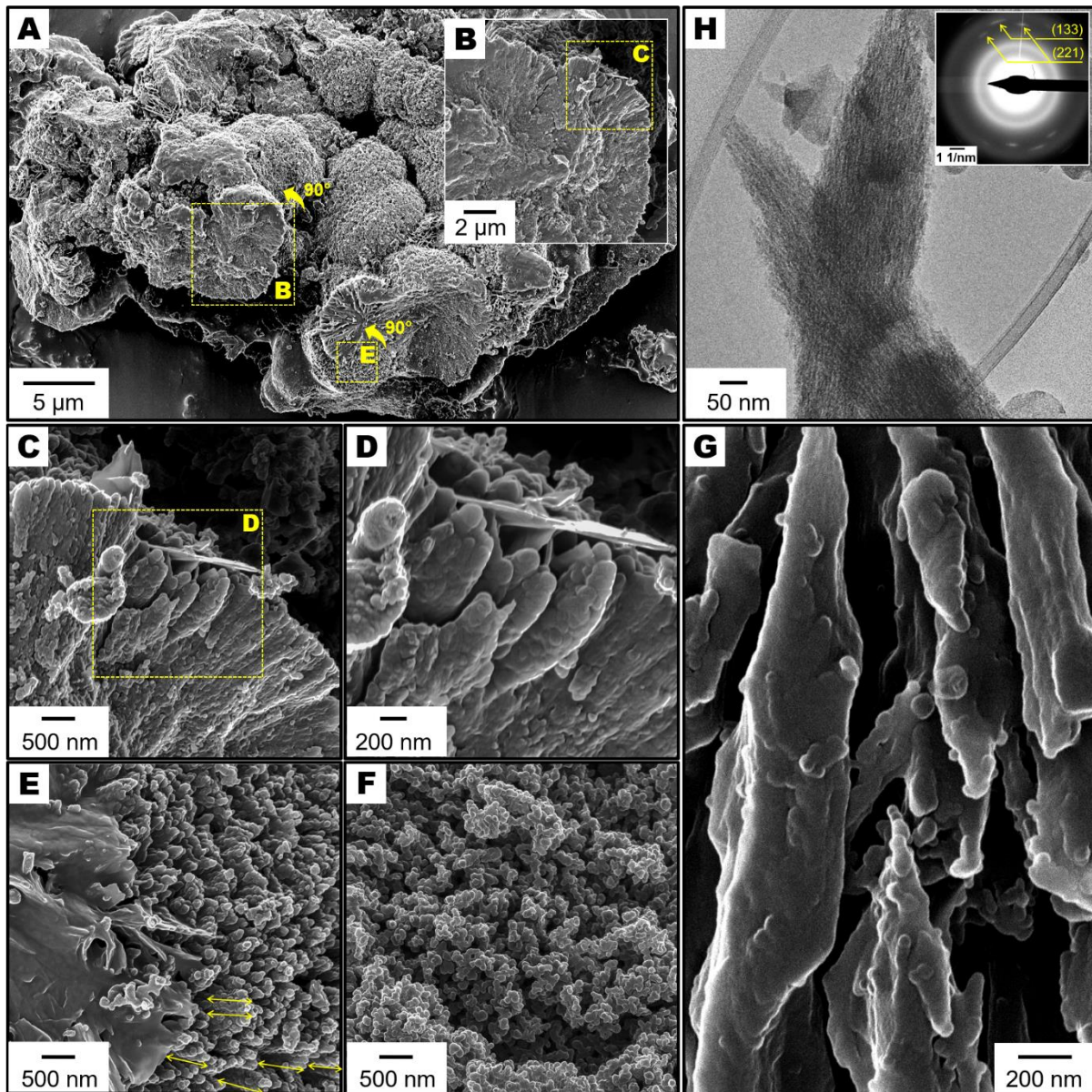
Figure 7.

Figure 7. Higher-order mineral structures following crystallization. Representative

scanning helium ion microscopy (SHIM) micrographs of the higher-order mineral structures

resulting from the crystallization of the synthetic, Amorphous Calcium Magnesium Carbonate

(ACMC) sample soaked in deionized water in the MAS rotor (**A** to **E**); and of the ACMC

nanoparticles shown before crystallization (**F**). (A) is a low magnification micrograph that

displays the presence of spherulitic aggregates. (B to D) and (E) are different micrographs at

higher magnifications that reveal the features of the monohydrocalcite crystals that compose

981 the spherulitic aggregates shown in (A). For the purpose of comparison with biogenic crystals

982 observed in coral skeleton, (**G**) shows a magnification of the square region marked by the

983 yellow dashed line drawn in **Fig. 1B**. This high magnification micrograph exposes the skeletal

984 fibers of a trabecula formed via a spherulitic growth mechanism [109], and shows the "nano-

985 particulate" texture of the acicular aragonite crystals. (**H**) Representative cryogenic

986 transmission electron microscopy (cryo-TEM) micrograph of the higher-order mineral

987 structures resulting from the crystallization of the synthetic ACMC sample soaked in

988 deionized water in a 10ml vial. Inset shows a selected area electron diffraction (SAED)

989 pattern of (H) labeled with monohydrocalcite crystal planes.

990　**Figure 8.**

991
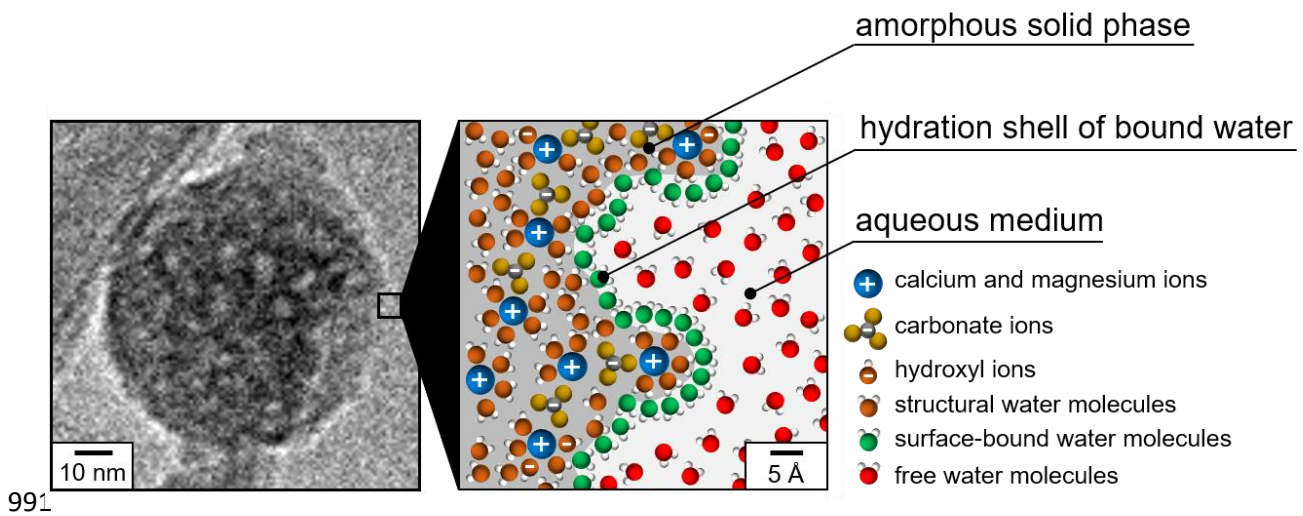
992　**Figure 8. Chemical and structural model of the synthetic amorphous nanoparticles.**

993　Representative cryogenic transmission electron microscopy (cryo-TEM) micrograph of a
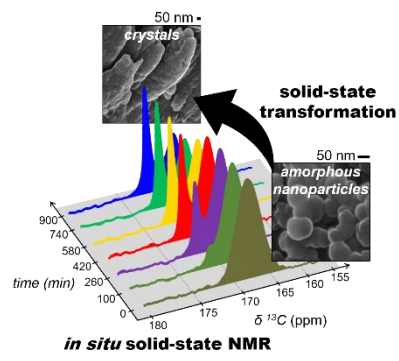
994　nanoparticle (diameter, about 80 nm) of the synthetic, Amorphous Calcium Magnesium

995　Carbonate (ACMC) sample dispersed in deionized water (**left**). Also shown is a two-

996　dimensional chemical and structural model of the surface region of an amorphous particle of

997　ACMC soaked in water (**right**).

998

999

1000   Table of Contents (TOC) image